

**CTIO, *ROSAT* HRI and *Chandra* ACIS Observations of the  
Archetypical Mixed-Morphology Supernova Remnant W28  
(G6.4–0.1)**

Thomas G. Pannuti<sup>1</sup>, Jeonghee Rho<sup>2,3</sup>, Oleg Kargaltsev<sup>4</sup>, Blagoy Rangelov<sup>4</sup>, Alekzander R.  
Kosakowski<sup>1,5</sup>, P. Frank Winkler<sup>6,7</sup>, Jonathan W. Keohane<sup>8</sup>, Jeremy Hare<sup>4</sup> and Sonny  
Ernst<sup>1</sup>

Received \_\_\_\_\_; accepted \_\_\_\_\_

---

<sup>1</sup>Space Science Center, Department of Earth and Space Sciences, Morehead State University, 235 Martindale Drive, Morehead, KY 40351, USA; E-mail: t.pannuti@moreheadstate.edu

<sup>2</sup>SETI Institute, 189 Bernardo Avenue, Mountain View, CA 94043, USA; E-mail: jrho@seti.org

<sup>3</sup>SOFIA Science Center, NASA Ames Research Center, MS 211-3, Moffett Field, CA 94035, USA; E-mail: jrho@sofia.usra.edu

<sup>4</sup>Department of Physics, 214 Samson Hall, George Washington University, Washington, D. C. 20052, USA; E-mail: kargaltsev@gwu.edu

<sup>5</sup>Homer L. Dodge Department of Physics and Astronomy, The University of Oklahoma, 440 W. Brooks Street, Norman, OK 73019; E-mail: alekzanderkos@ou.edu

<sup>6</sup>Department of Physics, Middlebury College, Middlebury, VT 05753, USA; E-mail: winkler@middlebury.edu

<sup>7</sup>Visiting Astronomer, Cerro Tololo Inter-American Observatory. CTIO is operated by AURA, Inc. under contract to the National Science Foundation.

<sup>8</sup>Department of Physics and Astronomy, Hampden-Sydney College, Hampden-Sydney, VA 23943, USA; E-mail: jkeohane@hsc.edu

## ABSTRACT

We present a joint analysis of optical emission-line and X-ray observations of the archetypical Galactic mixed-morphology supernova remnant (MMSNR) W28 (G6.4–0.1). MMSNRs comprise a class of sources whose shell-like radio morphology contrasts with a filled center in X-rays; the origin of these contrasting morphologies remains uncertain. Our CTIO images reveal enhanced [S II] emission relative to  $H\alpha$  along the northern and eastern rims of W28. Hydroxyl (OH) masers are detected along these same rims, supporting prior studies suggesting that W28 is interacting with molecular clouds at these locations, as observed for several other MMSNRs. Our *ROSAT* HRI mosaic of W28 provides almost complete coverage of the SNR. The X-ray and radio emission is generally anti-correlated, except for the luminous northeastern rim, which is prominent in both bands. Our *Chandra* observation sampled the X-ray-luminous central diffuse emission. Spectra extracted from the bright central peak and from nearby annular regions are best fit with two over-ionized recombining plasma models. We also find that while the X-ray emission from the central peak is dominated by swept-up material, that from the surrounding regions shows evidence for oxygen-rich ejecta, suggesting that W28 was produced by a massive progenitor. We also analyze the X-ray properties of two X-ray sources (CXOU J175857.55–233400.3 and 3XMM J180058.5–232735) projected into the interior of W28 and conclude that neither is a neutron star associated with the SNR. The former is likely to be a foreground cataclysmic variable or a quiescent low-mass X-ray-binary while the latter is likely to be a coronally-active main sequence star.

*Subject headings:* supernova remnants: individual (W28 (G6.4-0.1)) — supernova remnants: mixed morphology – interstellar medium: supernova remnants – X-rays:

interstellar medium

## 1. Introduction

A supernova remnant (SNR) is produced by the interaction between stellar ejecta released in the violent death of a star in a supernova explosion and the surrounding interstellar medium (ISM). SNRs play crucial roles in the evolution of the ISM of a galaxy through such processes as cosmic-ray acceleration and the deposition of vast amounts of kinetic energy and chemically-enriched material. Our understanding of SNRs has flourished in the modern era thanks to pointed observations made with space-based observatories such as *Fermi*, *Chandra* and *Spitzer*, which are capable of conducting highly sensitive imaging and spectroscopic observations of SNRs in the  $\gamma$ -ray, X-ray and infrared, respectively. Over 290 Galactic SNRs are known to exist (Green 2014) based on detections made at wavelengths across the whole electromagnetic spectrum. SNRs exhibit a range of morphologies at different wavelengths, which define distinct classes into which SNRs have been categorized: (1) Shell-like SNRs exhibit a shell of emission at both the X-ray and radio wavelengths, produced by an optically-thin plasma and synchrotron radiation, respectively. Well known examples include the young remnant Cas A and the more mature Cygnus Loop. (2) Crab-like SNRs, often known as plerions, feature center-filled morphologies in both X-ray and radio. At both wavelengths, the observed emission is synchrotron radiation from a nebula surrounding a dominant central pulsar. (3) A class of composite SNRs comprises sources that combine characteristics of the previous two classes, typically exhibiting both an exterior shell-like structure and a central pulsar-wind nebula. One well-studied example is CTB 80 (Safi-Harb et al. 1995).

A fourth class of SNR combines a shell-like radio morphology with a center-filled centrally-peaked X-ray morphology, but unlike the composite class, the central X-ray emission is not non-thermal in origin – as would be expected a pulsar-wind nebula – but is instead thermal and is produced by an optically-thin plasma. SNRs that belong to this class

are known as “mixed-morphology SNRs” (MMSNRs) (Rho & Petre 1998) or as “thermal composite” SNRs (Jones et al. 1998). MMSNRs typically feature temperature profiles that are relatively uniform, in contrast to the radially-dependent profiles predicted by the classical Sedov solution for SNRs expanding into a uniform ambient medium. Prominent examples of MMSNRs include W44, CTB 1, HB 3, HB 21 and G352.7–0.1 (Shelton et al. 2004; Lazendic & Slane 2006; Pannuti et al. 2010, 2014a).

A thorough understanding of the origin of the contrasting morphologies of MMSNRs remains elusive. In general, MMSNRs appear to be interacting with adjacent molecular clouds, as indicated by observations of strong infrared line emission from shocked molecules or OH masers (Frail et al. 1996; Reach & Rho 1996, 1998; Yusef-Zadeh et al. 2003). Therefore, it is believed that the interaction between the SNR and the molecular cloud dictates the creation of the contrasting morphologies, though a complete understanding of this phenomenon has not yet been realized. Numerous models have been proposed to explain the origins of the contrasting morphologies for MMSNRs (for reviews, see Chen et al. (2008), Vink (2012) and Zhang et al. (2015)). These models include: (1) enhanced internal gas density due to the evaporation of small and dense cloudlets that are overrun by the expanding shock of the SNR (McKee 1982; White & Long 1991); (2) a hot interior with an elevated density due to a thermal conduction (Cox et al. 1999; Shelton et al. 1999); (3) a radiatively cooled rim and a hot interior (Harrus et al. 1997; Rho et al. 1998); (4) an interaction between the SNR shock front and the edge of a cloud that appears brighter toward the projected interior of the SNR (Petruk 2001; Chen et al. 2004); (5) thermal conduction and enhanced emission from metals due to dust destruction and ejecta enrichment in the SNR interior (Shelton et al. 2004); and (6) reflection of the SNR blast wave off a wind-blown cavity created by the stellar progenitor, leading to a powerful reverse shock that heats the material in the SNR interior (Chen et al. 2008). None of these models can by themselves account for all of the observed properties of every known MMSNR, and

therefore more analyses of these sources is called for.

Recent spectroscopic X-ray analyses of MMSNRs have revealed the presence of ejecta-dominated emission as well as evidence that the X-ray-emitting plasmas associated with many MMSNRs are over-ionized. By “ejecta-dominated,” we mean that the elemental abundances of the X-ray emitting plasma are elevated relative to solar. While the presence of elevated abundances is expected for young SNRs that have not yet evolved past the free-expansion stage, MMSNRs have typical ages of between  $10^3$  to  $10^4$  years and should be well into the Sedov (adiabatic) stage of SNR evolution, dominated by swept-up interstellar matter. Zhang et al. (2015) compiled a list of approximately 30 MMSNRs for which elevated elemental abundances have been reported in the literature: this large number of sources indicates that MMSNRs may have a fundamentally different evolutionary path than the canonical model of SNR evolution that has been widely accepted in the literature. By “over-ionized,” we mean that the cooling rate of these X-ray-emitting plasmas is faster than the recombination rate. The ionization state of a plasma can be characterized by both its electron temperature  $T_e$  and its ionization temperature  $T_z$ , where the latter corresponds to the equilibrium temperature that would give the mix of ions observed spectroscopically. When  $T_e < T_z$ , the plasma is said to be underionized; when  $T_e > T_z$ , overionized; and when  $T_e = T_z$ , the plasma is said to be in collisional ionization equilibrium (see Miceli (2011) and Broersen & Vink (2015) for a more detailed description of the ionization conditions of the X-ray-emitting plasmas of SNRs).

The remarkable plasma conditions seen in MMSNRs – namely the presence of a plasma that appears to be both ejecta-dominated and overionized – have motivated investigations into how such a plasma may develop. Kawasaki et al. (2005) presented a scenario that predicts both the center-filled thermal morphology of MMSNRs and the overionization of the plasma. In this scenario, thermal conduction causes the X-ray-emitting plasma to

be center-filled: it also reduces the temperature and density gradients of the hot interior plasma, leading to a density increase and a temperature decrease: therefore, the plasma becomes overionized. This intriguing proposed scenario can adequately describe (in general terms) the observed properties of MMSNRs, but additional investigations are required to explore it (and its applicability to MMSNRs in general) more fully.

In this paper, we present optical and X-ray observations of the archetypical MMSNR W28 (G6.4–0.1) made with the Cerro Tololo Inter-American Observatory (CTIO) 0.6-meter Curtis Schmidt telescope, the High Resolution Imager (HRI) aboard *ROSAT* and the Advanced CCD Imaging System (ACIS) aboard the *Chandra* X-ray Observatory. The center-filled X-ray morphology of this SNR (Long et al. 1991; Rho et al. 1996) – coupled with its shell-like radio morphology (Dubner et al. 2000) – are well-known and clearly illustrate the morphological properties of MMSNRs. Radio observations of W28 have revealed a shell-like morphology with luminous northern and eastern rims as well as a tangential orientation to the magnetic field lines over the northern shell (Kundu 1970; Shaver & Goss 1970; Milne & Wilson 1971; Kundu & Velusamy 1972; Frail et al. 1994a; Dubner et al. 2000); a radio spectral index of  $\alpha=0.35\pm 0.18$  (where  $S_\nu \propto \nu^{-\alpha}$ ) for this source was measured by Dubner et al. (2000) using VLA data at 328 MHz and 1415 MHz. Narrow-band optical imaging of W28 (Long et al. 1991; Mavromatakis et al. 2004) shows patchy knots of emission, combined with extended diffuse emission, in both  $H\alpha$  and [S II] lines, especially in the central region where the X-rays are strongest. In addition, there are filaments of enhanced (relative to  $H\alpha$ ) [S II] emission – typical of material heated by SNR shocks – along the northern and eastern rims, coincident with the brightest portions of the radio shell. These regions also correspond to the sites of interaction between W28 and surrounding molecular clouds (see below).

W28 has been observed with virtually all the pointed X-ray missions, beginning with

the *Einstein* Observatory, where Long et al. (1991) discovered the centrally-peaked thermal X-ray emission from an SNR with a limb-brightened radio shell – the characteristics that have come to define MMSNRs. Rho & Borkowski (2002) analyzed *ROSAT* Position Sensitive Proportional Counter (PSPC) and *ASCA* observations of W28 and noted arcs of emission along the northeast and southwest portions of the shell, in addition to the brighter centrally peaked emission. They found that two thermal components were required ( $kT = 0.6$  keV and  $kT = 1.8$  keV) to fit the spectrum of the central diffuse X-ray emission. This was the first evidence for thermal variations in the emission from the interior of the SNR and makes W28 unique among MMSNRs. They also found that the arc of emission to the southwest had a hard thermal X-ray component, which they attributed to the breakout of the SNR shock opposite to the molecular clouds to the north and east. In their analysis of a pointed *Suzaku* observation made of W28, Sawada & Koyama (2012) fit the extracted spectra of the SNR with a multi-ionization-temperature plasma with a common electron temperature, where the multi-ionization temperatures are interpreted as elemental differences of ionization and recombination timescales. Such plasma conditions have not been identified in another MMSNR in the published literature.

Most recently, Zhou et al. (2014) and Nakamura et al. (2014) performed independent spectroscopic analyses of W28 based on *XMM-Newton* observations. Zhou et al. (2014) described complex conditions for the plasma at both the northeastern rim and the bright central region: the spectrum of the northeastern rim could be fit with either a combination of two thermal components or a thermal component combined with a power law component, while spectra from the central region could be fit with either two thermal components or a single recombining thermal model. They argued that W28 is expanding into a non-uniform environment with denser material to the east and north and that the cloudlet evaporation model may explain the observed properties of the X-ray emission from the center of the SNR while the thermal conduction model may play a role over large length scales that are

comparable to the radius of the SNR itself. Nakamura et al. (2014) concentrated on the northeastern region, where they showed a bright and twisted portion of the SNR shell to have X-ray emission that could be fit with a single temperature  $kT \approx 0.3$  keV optically thin plasma in ionization equilibrium. The emission measure requires a high density, consistent with the interaction with molecular clouds in that region.

There is abundant evidence published from other bands that W28 is interacting strongly with adjacent molecular clouds to the north and east. As noted previously, such a robust interaction with an adjacent molecular cloud seems to be a defining characteristic of MMSNRs. Based on observations of broad CO J=1-0 lines with a full-width at half-maximum (FWHM) of  $11 \text{ km sec}^{-1}$  and the presence of warm dense clouds, Wooten (1981) first suggested that W28 is interacting with adjacent molecular clouds. This result was confirmed through subsequent CO observations of the J=3-2 and J=1-0 lines that identified the presence of shock-excited masers along the northern and eastern rims of the SNR (Frail et al. 1994b; Frail & Mitchell 1998; Arikawa et al. 1999; Claussen et al. 1997, 1999; Hoffman et al. 2005; Hewitt et al. 2008). Mid-infrared observations of W28 from space-based observatories have also confirmed that W28 is interacting with nearby molecular clouds: using observations from the *Infrared Space Observatory*, Reach & Rho (2000) reported the detection of infrared S(3) and S(9) rotational lines of H<sub>2</sub>, along with strong emission in atomic fine-structure mid-IR lines, especially [O I]  $\lambda 64\mu\text{m}$ . Spectral fits indicate this emission originates from regions of density  $\sim 10^3 \text{ cm}^{-3}$ . In addition, Neufeld et al. (2007) and Marquez-Lugo & Phillips (2010) presented spectroscopic and imaging observations, respectively, made of W28 with the *Spitzer* Space Telescope. The former paper described the spectroscopic detection of both a shock-excited component and a low-density diffuse emission component for the H<sub>2</sub> S(0) line, while the latter paper presented an analysis of the spectral energy distributions of Class I young stellar objects (Lada 1987) seen in projection toward the northwestern interaction region of W28 and suggested that

the formation of these sources may have been triggered by the supernova event associated with this SNR.

Finally, high-energy  $\gamma$ -ray emission has been detected from W28 by *Fermi* (Abdo et al. 2010) and H.E.S.S. (Aharonian et al. 2008): modeling of this emission by those authors and Li & Chen (2010) favor a hadronic origin where energetic protons collide with molecular clouds, again supporting the scenario that W28 is indeed interacting with adjacent molecular clouds. The totality of evidence that the SNR shock in W28 is interacting with one or more molecular clouds in the north and east is compelling. In this paper, we will consider high angular resolution optical and X-ray observations of W28 with the goal of analyzing its high energy emission on fine spatial scales and testing the applicability of the different models in explaining its X-ray properties.

As is the case for many Galactic SNRs, the distance to W28 is poorly known, with estimates ranging between 1.6 and 3 kpc (Clark & Caswell 1976; Milne 1979; Frail et al. 1994a). For the present paper, we note that CO observations of the shock interaction between W28 and an adjacent molecular cloud imply a distance of 1.8 kpc (Arikawa et al. 1999) based on the rotation curve for a Sun-Galactocentric distance of 8.5 kpc (Clemens 1985). We therefore adopt this distance to W28; we note that this choice of distance is consistent with our previous X-ray study of W28 (Rho & Borkowski 2002).

The present paper is organized as follows: in Section 2 we describe the observations that were incorporated into our study, beginning with the optical observations made with the CTIO 0.6-meter Curtis Schmidt telescope (Section 2.1) and continuing with high angular resolution X-ray observations made with the *ROSAT* High Resolution Imager (HRI) (Section 2.2) and the *Chandra* Advanced CCD for Imaging and Spectroscopy (ACIS) (Section 2.3). Our imaging and spectral analyses of the datasets are presented in Section 3: we discuss our narrowband optical images in Section 3.1, our *ROSAT* HRI mosaic of

W28 in Section 3.2, our spatially resolved X-ray spectroscopic analysis using *Chandra* in Section 3.3, and the morphologies of W28 at different wavelengths in Section 3.4. In Section 4 we discuss X-ray emission from two particular discrete X-ray sources seen toward W28, namely CXOU J175857.55–233400.3 (a hard X-ray source seen in prior *ASCA* observations of W28 as reported by Rho & Borkowski (2002)) and 2XMM J180058.6–232724 = 3XMM J180058.5–232735 (a discrete X-ray source seen toward the geometric center of W28). The analyses of these sources is conducted to determine if either source may be an X-ray-emitting neutron star that is physically associated with W28. Finally, the conclusions of this paper are presented in Section 5.

## 2. Observations

In this Section, we present a brief description of the observations (as well as the corresponding data reduction) for the CTIO, *ROSAT* HRI and *Chandra* ACIS observations of W28. In addition, in our analysis we also make use of a 1415 MHz radio map of W28 based on VLA data: this map was kindly provided to us by G. Dubner, and details about this map can be found in Dubner et al. (2000).

### 2.1. Optical Observations

We obtained optical images of W28 from the CTIO 0.6-m f/3.5 Curtis Schmidt telescope on the night of 1998 June 22 (UT). The telescope was equipped with the SITE2K#5 CCD, mounted at Newtonian focus, to give a field 1:32 square at a scale of 2:32 pixel<sup>-1</sup>. We used narrow-band interference filters centered on the H $\alpha$  and [S II] emission lines, plus a matched line-free continuum filter for subtracting the stars to better reveal faint nebulous emission. The observational details are given in Table 1. The data were processed using

conventional IRAF<sup>1</sup> techniques, including bias subtraction and flat-fielding using a series of well-exposed twilight sky flats. A World Coordinate System, based on stars from the UCAC1 catalog (Zacharias et al. 2000), was placed on each individual frame; all the frames were then transformed to a common system at a finer scale of  $1'' \text{ pixel}^{-1}$  and stacked by filter. The continuum image was scaled appropriately and subtracted from the H $\alpha$  and [S II] ones to effectively remove most of the stars. The final images were flux-calibrated based on observations of several spectrophotometric standard stars from the list of Hamuy et al. (1992).

## 2.2. *ROSAT* HRI Observations

W28 was the subject of nine pointed *ROSAT* HRI observations conducted between 20 March 1995 and 11 September 1998 that sampled the entire X-ray extent of the SNR. The HRI was sensitive to photons over the energy range between 0.1–2.4 keV and had a field of view  $36'$  square (see Zombeck et al. 1995, for details). With an angular size of  $\sim 48'$  (Green 2014), W28 is larger than the HRI field; hence we generated a mosaicked image of W28 with data from the individual exposure-corrected HRI observations. We used the techniques described by Snowden (1998) for analyzing *ROSAT* HRI images and the Extended Source Analysis Software (ESAS<sup>2</sup>) which was created by S.L. Snowden and K.D. Kuntz of Goddard Space Flight Center. Images were prepared from the nine individual observations by first casting the observed events, the exposure maps and the background maps into images, and then using these images to generate intensity images for each individual observation.

---

<sup>1</sup>IRAF is distributed by the National Optical Astronomy Observatories, which is operated by the AURA, Inc. under cooperative agreement with the National Science Foundation.

<sup>2</sup>Obtained from `ftp://legacy.gsfc.nasa.gov/rosat/software/fortran/sxrb/`.

Six of the nine observations were “broken exposures” which sampled the same region of W28 more than once; that is, the central, southern and southeastern portions of W28 were each observed twice (see Table 2 for details). Before making the mosaic image, we summed each pair of broken exposures to make total intensity images, exposure maps and background maps for these three portions of W28. We then mapped the counts, exposures and background counts from the projection of the individual exposures into the mosaic projection. We next calculated the Long-Term Enhancement – that is, the intrinsic HRI background (Snowden 1998) – for each exposure (or pair of broken exposures): this step determines the relative offsets in the zero levels of the observations to be merged. We made a mosaicked image of the modeled offset counts and then finally a mosaicked final count rate image (with a pixel size of  $12''$ ) using the individual counts, the modeled background counts, the modeled offset counts and the exposure maps for each individual exposure (or pair of broken exposures). We adaptively smoothed the full mosaicked rate map, using a smoothing kernel of 30 counts for the adaptive filtering algorithm.

### 2.3. *Chandra* ACIS Observations

W28 was observed with the ACIS detectors on the *Chandra* X-ray Observatory on 12 October 2002 (ObsID 2828; PI Rho). The pointing placed the back-illuminated S3 chip (which has enhanced soft X-ray sensitivity) on the brightest portion of the central emission; the adjacent S2 and S4 chips sampled other portions of the central emission, while two ACIS-I chips sampled emission in the southwest of W28, where the hardest emission is located (Rho & Borkowski 2002). Data were processed with CIAO version 4.8 (CALDB Version 4.7.2), beginning with the CIAO tool `chandra_repro` to assure that the latest calibrations were applied. We further filtered the resulting events file to exclude periods with significant background flare activity, resulting in a net effective exposure time of 88994

seconds. In Table 2 we present a summary of the *Chandra* observation of W28.

To perform a spectral analysis of the X-ray-emitting plasma associated with W28, we divided the field of view of the ACIS-S3 chip into multiple regions and used the CIAO tool `specextract` to generate the files – source spectra, background spectra, ancillary response files (ARFs) and redistribution matrix files (RMFs) – that are necessary for spectral analysis. We considered diffuse emission from W28 as sampled by the ACIS-S3 and -S4 chips during these observations: no diffuse emission was detected at a significant level from W28 by the ACIS-S1 chip during this observation and we do not consider that chip in the present paper. Because the entire S3 chip was filled by diffuse emission from W28, a blank sky observation was used to extract background spectra: the pointer header keyword values from the observation of W28 were applied to the blank sky observation file. The blank sky observation file was also then reprojected to match the projection of the ACIS chip: the same region used for source spectrum extraction in the W28 dataset was used in the reprojected blank sky dataset to obtain background spectra. The extracted spectra were grouped to a minimum of 25 counts per channel. To reduce the effect of point source contamination on the extracted spectra (from background sources or Galactic stellar sources seen in projection toward W28), the CIAO tool `wavdetect` was used to identify unresolved sources detected by the *Chandra* observation. Fluxes from the positions of these identified point sources were excluded when analyzing the extracted diffuse emission. Analysis of the extracted spectra was conducted using the XSPEC software package (Arnaud 1996) Version 12.9.0n.

### 3. Analysis and Results

#### 3.1. Narrow-band Optical Images of W28

In Figure 1 we show the optical images of W28 in the  $H\alpha$  and [S II] emission lines, after continuum subtraction to remove most of the stars in this highly congested field and to better reveal faint nebulous emission. The images in both lines show the same patchy diffuse emission in the central portion of W28 seen in previous optical images (Long et al. 1991; Mavromatakis et al. 2004). In addition, there is more filamentary emission, especially near the northern and eastern rims of the shell, that is stronger in [S II] relative to  $H\alpha$  – as is typical of SNR shocks. The differences between the two bands are more apparent in the two color Fig. 2, where  $H\alpha$  is shown in red and [S II] in green. The identical image is also shown in Fig. 3, overlaid with radio contours from Dubner et al. (2000). The locations of OH masers – signposts of interaction between an SNR and a molecular cloud – as detected by Claussen et al. (1999) are indicated with magenta crosses: notice how the locations of the masers more strongly correlate with the locations of high [S II] emission. Such a correlation may be expected, given that elevated [S II] emission relative to  $H\alpha$  is a known tracer of SNR shocks. There is a particularly dense concentration of masers seen toward the northeastern rim (also known as an “ear”-like structure of emission – see Rho & Borkowski (2002)): this rim – which is also detected in the X-ray and radio – is also detected prominently in the [S II] image.

#### 3.2. *ROSAT* HRI Mosaic

To help provide a context about the observed morphologies of W28 at different wavelengths, in Figures 4 and 5 we present radio and X-ray images, respectively, of the SNR. The shell-like radio morphology of the SNR is apparent, and the SNR appears

to be brightest along its northern and eastern rims, where the SNR is interacting most dramatically with adjacent molecular clouds, as indicated by the positions of the OH masers. The X-ray map was made using the *ROSAT* PSPC and was published by Rho & Borkowski (2002). Inspection of these two figures helps to illustrate the stark contrast in morphologies at the two wavelengths. The X-ray emission from W28 appears to be centrally concentrated at approximately RA (J2000.0)  $18^h 00^m 26.^s5$  and Decl. (J2000.0)  $-23^\circ 24' 24''$  with faint diffuse extensions filling much of the interior volume of W28. The only feature seen in both the X-ray and the radio is the bright northeastern rim which is also prominent in the [S II] image and the site of a high concentration of masers, as described in the previous section.

In Figure 6 we present our *ROSAT* HRI mosaic image of W28, which covers the entire angular extent of the SNR. Like the *ROSAT* PSPC image in Figure 5, this image demonstrates the centrally-concentrated nature of the X-ray emission from the SNR. With its angular resolution superior to that of the PSPC, the mosaicked HRI image shows more clearly the difference between emission in the X-ray and radio bands. Zhou et al. (2014) presented a mosaicked *XMM-Newton* image of W28 with comparable angular resolution to this mosaicked image and describe the X-ray morphology of the SNR in their image in similar terms.

### 3.3. *Chandra* Imaging and Spectra of Individual Regions

In Figure 7 we present an exposure-corrected, adaptively smoothed, three-color *Chandra* image of W28: the red, green and blue emission correspond to soft, medium and hard X-ray emission which in turn correspond to the energy ranges of 0.5 keV - 1.2 keV, 1.2 keV - 2.0 keV and 2.0 keV - 7.0 keV, respectively. As indicated by previous X-ray observations of W28, the emission is centrally concentrated: the “yellow” nature of the

emission detected from the central region indicates that this emission is not entirely soft (which is typical for SNRs) but that harder emission is present in this region as well. A clear decreasing gradient in brightness is seen in the direction toward the radio rim of the SNR: the centrally-peaked emission and decreasing brightness gradient are typical of MMSNRs like W28. Toward the southwestern portion of the SNR, the hard emission detected and described by Rho & Borkowski (2002) appears to be concentrated into a single discrete hard X-ray source. The true angular extent of this source is hard to determine given the elongation of the point spread function of *Chandra* for an object located so far from the optical axis of the telescope. A more detailed discussion of this source is provided in Section 4.

We conducted a spatially-resolved spectroscopic analysis of the X-ray emission from W28 in three different steps: we extracted and fitted spectra for the bright central peak that was located on the ACIS-S3 chip during the observation, for five individual regions located on the ACIS-S3 chip and one region on the ACIS-S4 chip (this latter region appears to be associated with both strong radio and [S II] emission along with pronounced “yellow” X-ray emission) and for eight annular regions located on the ACIS-S3 chip that are centered on the bright central X-ray peak along with the region on the ACIS-S4 chip. Below we present and discuss the results of these fits below in turn.

### *3.3.1. Spectrum of Bright Central Peak*

First, we extracted a spectrum from the central peak of emission and used XSPEC to fit the extracted spectra with different thermal models: (1) two thermal plasmas in collisional ionization equilibrium with different temperatures and with variable elemental

abundances (VAPEC+VAPEC)<sup>3</sup>; (2) two thermal plasmas in non-equilibrium ionization with different temperatures and with variable elemental abundances (VNEI+VNEI); (3) a more sophisticated model of a single thermal recombining plasma with variable elemental abundances, where the plasma is assumed to have started in collisional equilibrium with the initial temperature  $kT_Z$  and currently has an electron temperature  $kT_e$  (VRNEI); and finally (4) two thermal recombining plasmas with variable elemental abundances and different values of  $kT_Z$  and  $kT_e$  (VRNEI+VRNEI). The reader is referred to Borkowski et al. (2001) for a thorough description about non-equilibrium ionization models. Note that non-equilibrium models are characterized by the ionization timescale parameter  $\tau$ : this parameter – which is the product of the electron number density  $n_e$  and a timescale  $t$  – indicates whether or not the X-ray emitting plasma is in collisional ionization equilibrium. In the cases where two thermal models were used simultaneously (namely the VAPEC+VAPEC fit, the VNEI +VNEI fit and the VRNEI+VRNEI fit), the elemental abundances of the two models were tied together. All of these thermal models were multiplied by the Tübingen-Boulder interstellar medium absorption model TBABS to account for absorption along the lines of sight. For elemental abundances, we adopted the set from Wilms et al. (2000).

The region of spectral extraction for the bright central peak is shown in Figure 8. In Table 3 we present the results of our fitting: we find that only the TBABS×(VRNEI+VRNEI) model provides a statistically-acceptable fit to the extracted spectrum. The fit with the TBABS×(VRNEI+VRNEI) model yields two low-temperature thermal components ( $kT_{e1} = 0.10$  keV and  $kT_{e2} = 0.42$  keV): the corresponding  $kT_Z$  values for these thermal plasmas are 0.16 keV and 3.08 keV, respectively. Neither of these thermal plasmas are in collisional

---

<sup>3</sup>This model is based on a variable elemental astrophysical plasma emission code (APEC). For more information about this code, see Smith et al. (2001) and [http : //www.atomdb.org](http://www.atomdb.org).

ionization equilibrium ( $\tau_1$  and  $\tau_2$  are both significantly less than  $10^{12} \text{ cm}^{-3} \text{ s}$ ). During the fitting processes, the abundances of different elements were allowed to vary: we found that only the abundances of oxygen, neon, magnesium and iron showed evidence for being either underabundant or overabundant relative to solar. When the abundances of magnesium, silicon, sulfur, argon and calcium were allowed to vary, we found no evidence that the abundances of any of these elements were significantly different from solar: therefore, we left the abundances of these elements frozen to unity during the fitting process. The fit with the TBABS $\times$ (VRNEI+VRNEI) model exhibits elemental abundances of oxygen, neon and iron to all be subsolar: this result indicates that the X-ray emission from the bright central peak is dominated swept-up ISM rather than stellar ejecta. We present fits to the extracted spectrum of this bright central region using these four models in Figure 9. Our results are broadly consistent with other published spatially-resolved X-ray spectroscopic analysis of W28: for example, Sawada & Koyama (2012) used multiple VRNEI components to obtain a statistically-acceptable fit to the extracted *Suzaku* XIS spectra of the SNR.

### 3.3.2. Spectra of Five Regions on the ACIS-S3 Chip and A Region on the ACIS-S4 Chip

The second step of our spatially-resolved spectroscopic analysis of the X-ray emission from W28 was to extract and fit spectra from five regions seen toward the central bright emission of the SNR on the ACIS-S3 chip and a region on the ACIS-S4 chip. These regions are shown in Figure 10: we refer to these as Regions 1 through 5 along with the ACIS-S4 chip region for the remainder of this paper. The spectra from the five regions on the ACIS-S3 chip were fitted over the energy range from 0.5 to 4.0 keV while the spectrum from the region on the ACIS-S4 chip was fitted over the energy range from 0.6 to 2.0 keV due to poorer statistics in this spectrum. These spectra were fitted with three different thermal models: VNEI, VRNEI, and VRNEI+VRNEI. We first compare the fits made with

the VNEI and the VRNEI models. In fitting the spectra with these two models, the column density for all of the regions was tied together and treated as a single parameter: we found that fitting the column densities individually for the five regions produced no statistically significant differences in the fits. In all the fits, the elemental abundances of oxygen and iron were allowed to vary, while the elemental abundances of the other elements were frozen to solar values. The results of these spectral fits using the VNEI and VRNEI models are presented in Tables 4 and 5. We find that the VRNEI model provides a superior fit to the spectra than the VNEI model: we interpret this result to indicate that the X-ray emitting plasma associated with W28 is best described on small spatial scales by an overionized recombining plasma.

Finally, in Table 6, we present the results of fitting the spectra with a TBABS×(VRNEI+VRNEI) model where again the column density for all of the regions was tied together and treated as a single parameter. We have also allowed the abundances of neon to vary as well as oxygen and iron. We find that – when comparing the values of  $\Delta\chi^2$  for these fits to the fits presented in the previous tables – the VRNEI+VRNEI model produces a greatly improved fit result with a dramatically reduced value of  $\Delta\chi^2$  down to 1.24. In Figure 11, we show the spectra of these six regions as fit with the TBABS×(VRNEI+VRNEI) models and the contributions of the two individual thermal components in each fit are shown.

We also find evidence of enhanced elemental abundances of oxygen relative to iron in the extracted *Chandra* spectra of W28: this result lends support to the scenario that W28 was produced by a massive stellar progenitor (Woosley & Weaver 1995; Nomoto et al. 1997). In previous work, we have used the ratio of oxygen to iron elemental abundances as seen in the extracted *Chandra* spectra of the MMSNR CTB 1 (G116.9+0.2) to estimate the progenitor mass as 10 and 15  $M_{\odot}$  – see Pannuti et al. (2010)). By inspection of

the parameters of the fits presented in Tables 4 through 6, it appears that the ratios of the elemental abundances of oxygen to iron (relative to solar abundances) range up to approximately 3: this result is broadly similar with the results of our spectral fitting for CTB 1 and suggests that the progenitor had approximately the same mass. This result lends support to the scenario that W28 had a massive stellar progenitor and that – as a class – MMSNRs tend to stem from massive stellar progenitors.

Our spectral fitting results are again consistent with the analysis of extracted *Suzaku* spectra of W28 as presented by Sawada & Koyama (2012): the superior angular resolution of *Chandra* allows us to probe the properties of the plasma on much smaller spatial scales.

### 3.3.3. *Spectra of Annular Regions on the ACIS-S4 Chip and A Region on the ACIS-S4 Chip*

Lastly, we discuss our analysis of spectra extracted from annular regions centered on the bright central peak of X-ray emission on the ACIS-S3 chip along with the region on the ACIS-S4 chip. As described elsewhere, MMSNRs are known to feature uniform temperatures in their interiors which is believed to result from thermal conduction (Shelton et al. 2004; Vink 2012). Furthermore, detailed magnetohydrodynamic simulations of the evolution of MMSNRs predict that thermal conduction in the interiors of these sources will facilitate a steep metallicity gradient in the extracted X-ray spectra of the SNR (Orlando et al. 2009). To search for variations in temperatures and metallicities as a function of radius in the central thermal X-ray emission, we extracted and fit spectra from eight annular regions (each with a thickness of approximately 25 arcseconds) that centered on the bright X-ray peak located on the ACIS-S3 chip. The annular regions of spectral extraction are shown in Figure 12: note that these regions extend nearly to the edge of the chip itself.

The spectra of the annular regions were fit simultaneously with the spectrum from the ACIS-S4 region with a TBABS×VRNEI model. The abundances of oxygen and iron were allowed to vary while the abundances of the other elements were frozen at solar. The results of these fits are presented in Table 7. We find that the values for electron temperature  $T_e$  remain approximately constant for all of the regions (as seen in other MMSNRs): however, as indicated by the fitted abundances of oxygen and iron for all of the regions, we find no evidence for a gradient in metallicity in the X-ray-emitting spectra. In predicting the presence of such a gradient, Orlando et al. (2009) argue that such a gradient would be due to a reverse shock propagating inward and confining the ejecta to the inner part of the SNR. It is possible that in the evolution of W28, a reverse shock propagating inward has not established this gradient: the absence of the gradient may be due to the complex ambient ISM into which W28 is expanding. Additional observations and analysis are needed to explore this result further.

### 3.4. Spatial Comparison of X-ray, Optical and Radio Emission from W28

We have presented a comparison of the spatial morphologies of W28 at X-ray, optical and radio wavelengths. As the archetypical MMSNR, W28 features a shell-like radio morphology with a contrasting center-filled X-ray morphology: this X-ray morphology is defined by thermal emission. The only spatial feature that is detected at all three wavelengths is the northeastern “ear,” where the W28 shock appears to be interacting strongly with an adjacent molecular cloud, and where there is a high density of OH masers (Claussen et al. 1997). The detection of emission at multiple wavelengths from particular features of an MMSNR underscores that such features may be sites of particularly vigorous interactions between the SNR and the adjacent molecular clouds.

We note that the optical morphology of W28 exhibits an important contrast in

comparison with the optical morphologies of other MMSNRs. In general, the optical morphologies of MMSNRs resemble their radio morphologies in that they are shell-like in appearance: examples of well-known MMSNRs with shell-like optical morphologies include CTB 1 (G116.9+0.2) and CTA 1 (G119.5+10.2) (see Fesen et al. (1997) and Mavromatakis et al. (2000), respectively). As described previously, the optical morphology of W28 is not shell-like but instead center-filled, exhibiting central diffuse “puffy” structure: in this sense, the optical morphology resembles that of another MMSNR – HB21 (G89.0+4.7) – that features both shell-like filamentary structure that is coincident with radio emission along with patchy emission toward the SNR interior (Mavromatakis et al. 2007). Like HB21, the optical morphology of W28 may be sculpted by a complex interstellar medium into which the SNR is expanding.

#### 4. Discrete X-ray Sources

We now present a discussion about the two most prominent X-ray sources in the W28 field and investigate whether either could be a neutron star associated with this SNR. Searches for compact objects in MMSNRs are of particular interest because so far only two of the 25 MMSNRs listed in Table 4 of Vink (2012) have firmly associated neutron stars.<sup>4</sup> Hence, either most of these SN explosions leave no compact object, which seems unlikely if these SNRs had massive stellar progenitors as commonly assumed, or the compact objects are isolated, non-accreting black holes. The latter scenario seems more likely for SNRs in molecular clouds, since their massive progenitors could have had lifetimes shorter than those of the clouds that produced them. Establishing the number of SNRs with black

---

<sup>4</sup>The specific MMSNRs are W44 and IC 443 with their associated neutron stars PSR B1853+01 and CXOU J061705.3+222127, respectively (Petre et al. 2002; Swartz et al. 2015).

hole compact objects provides constraints on stellar evolution theory, supernova explosion mechanisms and the mass function for massive stars. To date, no neutron star has been conclusively associated with W28: the pulsar PSR B1758–23 (Manchester et al. 1985) was once thought to be associated with the SNR (Frail et al. 1993) but this association was later discarded based on VLBA measurements of the interstellar scattering in the direction of the pulsar (Claussen et al. 1999) along with a large observed dispersion of the pulsar signal that cannot be reconciled easily with independent distance estimates to W28 (Kaspi et al. 1993).

The first source of particular interest to us – CXOU J175857.55–233400.3 – appears to be the source of the hard X-ray emission detected from the southwest portion of W28 by the prior *ASCA* observations of the SNR that were presented by Rho & Borkowski (2002). Those authors noted that the hard X-ray emission detected from W28 seemed to be localized to this portion of the SNR; the *Chandra* observation presented here seems to favor a resolved source strongly smeared out by the broad off-axis PSF. The other X-ray source – 3XMM J180058.5–232735 – is the brightest X-ray source near the center of W28. The locations of both of these sources are indicated in Figure 7.

#### 4.1. CXOU J175857.55–233400.3

This source was imaged by the *Chandra* ACIS nearly  $22'$  off-axis, and hence an analysis of the properties of this source is severely impacted by the PSF degradation. CXOU J175857.55–233400.3 may be a true point source smeared out due to the broadened PSF and embedded in faint diffuse emission from the SNR, which makes it appear more asymmetric and different in shape from what might be expected from simple PSF broadening. Alternatively, the extended emission may be intrinsic to the source. The peak in brightness of the source is located at R.A.= $17^{\text{h}}58^{\text{m}}57^{\text{s}}.55$  and Decl.= $-23^{\circ}34'00.3''$  with a  $1\sigma$  uncertainty of  $\approx 15''$  (estimated as in Pavlov et al. (2009)). We extracted 1770

photons from a circle with a radius  $r = 22''$  (corresponding to the encircled source fraction of about 75%) centered at the peak of the source surface brightness: of these counts, 54% come from the surrounding background. The spectrum is shown in Figure 13 (left panel): a statistically-acceptable fit ( $\chi_\nu=1.05$  for 14 degrees of freedom) is obtained using an absorbed power law (PL) model with a photon index  $\Gamma = 0.47 \pm 0.25$  and a hydrogen absorption column density<sup>5</sup>  $N_H = (0.9 \pm 0.4) \times 10^{22} \text{ cm}^{-2}$ . The absorbed and unabsorbed fluxes for the source are  $(4.1 \pm 0.2) \times 10^{-13} \text{ ergs cm}^{-2} \text{ s}^{-1}$  and  $\approx 4.7 \times 10^{-13} \text{ erg cm}^{-2} \text{ s}^{-1}$ , respectively.

We cross-correlated the position of CXOU J175857.55–233400.3 with those of IR sources within a  $15''$  distance using standard Vizier catalogs. There are a total of 56 sources within this radius in the UKIDSS-DR6 catalog (with J-magnitude range of  $\approx 13 - 20$ ; a J=13 mag source is  $11''$  away from the X-ray source position) and 23 *Spitzer* IRAC sources (IRAC band 1 magnitudes range is  $\approx 11 - 14.5$ ; the nearest source is  $4.5''$  away from the X-ray source position). The closest counterpart (UGPS J175857.43–233357.4) found was in the UKIDSS-DR6 catalog at a distance of  $1.8''$  from CXOU J175857.55–233400.3, while the next closest UKIDSS source is  $2.6''$  away and is dimmer by about 1 mag; others are beyond  $4''$  away. Trying to classify CXOU J175857.55–233400.3 by assuming all possible combinations of IR and NIR counterparts within  $15''$  radius would be a very laborious task. To obtain much more certain results, it is necessary to conduct a short ( $\sim 10$  ks) on-axis *Chandra* observation to pin down the position of the X-ray source to arcsecond precision.

Nonetheless, if we assume that the nearest UKIDSS source (with magnitudes  $J = 18.5 \pm 0.1$ ,  $17.2 \pm 0.1$ , and  $16.7 \pm 0.1$ ; not detected in IR) is the actual counterpart to CXOU J175857.5–233400.3, then this source would have a very large  $F_X/F_{\text{NIR}}$  ratio for a coronally active star (see Figure 14; these conclusions would not change if the second nearest UKIDSS source were the actual counterpart). A Wolf-Rayet (non-binary) star

---

<sup>5</sup>We used the `phabs` model from XSPEC.

would have a much softer X-ray spectrum than that extracted for this source and it would appear to be bright in the infrared (specifically in the *Spitzer* IRAC bands) at the extinction inferred from X-ray spectral fits that place CXOU J175857.5–233400.3 closer than the Galactic center. The nondetection of UGPS J175857.43–233357.4 by the *Spitzer* IRAC (at the 8 micron band) and MIPS (at the 24 micron band) suggests that the source is not a young stellar object (YSO) or protostar. Such objects usually cluster together, and we do not see other X-ray sources with similar X-ray spectra within the immediate vicinity. Confident identification of this X-ray source with a NIR counterpart would further exclude classification of the source as an isolated neutron star – which is already unlikely given the very hard spectrum of the source. The remaining possible classifications of this X-ray source are as a cataclysmic variable (CV) or a quiescent low-mass X-ray binary. These are supported by the location of CXOU J175857.55–233400.3 in the diagrams shown in Figure 14. Emission is detected at a longer wavelength (0.87 mm) in an ATLASGAL (0.87 mm) image at a location north of CXOU J175857.55–233400.3 and at radio wavelengths (20 cm and 90 cm) larger-scale regions of enhanced emission stretching from north to south are detected. In Figure 15 we present multiwavelength (chiefly infrared and radio) images of the neighborhood surrounding CXOU J175857.55–233400.3.

#### 4.2. 3XMM J180058.5–232735

This X-ray source is of a particular interest because it is located close to the geometric center of W28 and is relatively bright. Although it lies outside the *Chandra* footprint, it is seen in several *XMM-Newton* observations listed in the 3XMM-DR5 catalog (Rosen et al. 2016), but always relatively far off-axis (12′–15′). Nevertheless, it has a well-determined position with  $1\sigma$  uncertainty of 0.6″ in the 3XMM-DR5 catalog. In this paper, we will adopt the coordinates for this source to be R.A.=18<sup>h</sup>00<sup>m</sup>58<sup>s</sup>.59 and Decl.=−23°27′35 9″

(J2000.). There is a fairly bright optical/NIR/IR counterpart detected in the only  $\approx 0.4''$  from the 3XMM position. The UCAC4 Catalog (Zacharias et al. 2013) lists magnitudes for this star (UCAC4-333-134563) as  $B=14.45$ ,  $V=13.44$ ,  $R=13.11$  and  $I=12.69$ , while UKIDSS-DR6 magnitudes are  $J = 11.23$ ,  $H = 11.02$ , and  $K = 10.66$ . Finally, the infrared counterpart detected by the WISE all-sky survey has magnitudes  $W1 = 9.80$ ,  $W2 = 9.80$ , and  $W3 = 9.27$ . The colors indicated by these counterparts are used to plot the location of 3XMM J180058.5–232735 in the diagrams shown in Fig. 14. The presence of a bright counterpart to the X-ray source at optical, near-infrared and infrared wavelengths – coupled with the locations of the X-ray source within the color-color diagrams – tend to rule out classification of 3XMM J180058.5–232735 as a background AGN or a neutron star or pulsar. The most likely classification of this X-ray source is as a relatively nearby foreground star with an active corona. This classification is supported by the large proper motion of UCAC4-333-134563:  $\Delta RA = -24.2 \pm 2.0$  mas yr $^{-1}$  and  $\Delta Decl = 11.5 \pm 5.6$  mas yr $^{-1}$ . Furthermore, the automated classification algorithm for X-ray sources described by Sonbas et al. (2016) and Hare et al. (2016) favors a classification of the source as either a coronally-active main-sequence (MS) star or a YSO.

We fitted an absorbed power law model to the source spectrum (extracted from XMM EPIC-PN data for ObsID 0135742201). The spectrum is shown in Figure 13 (right panel). The best-fit absorbed PL parameters are  $N_H = (3.2 \pm 1.5) \times 10^{21}$  cm $^{-2}$  and  $\Gamma = 3.8 \pm 1.3$ . The spectrum is soft and consistent with active coronae spectra: the small number of counts and low signal-to-noise preclude any more detailed spectral fitting.

## 5. Summary and Conclusions

The conclusions of this paper may be described as follows:

1) We present and analyze for the first time optical (CTIO) and X-ray (*Chandra* ACIS and *ROSAT* HRI) imaging observations of the archetypical mixed-morphology SNR W28. These observations have allowed us to analyze X-ray emission from this SNR with the highest angular resolution yet (approximately  $12''$  for our *ROSAT* HRI mosaicked image of W28 and as high as  $1''$  for the portions of W28 sampled by *Chandra*.)

2) The new narrowband [S II] and  $H\alpha$  optical images of W28 reveal extensive diffuse structure with patchy knots and filaments. The [S II] emission is strongest relative to the  $H\alpha$  emission along the northern and eastern rims of the SNR; large numbers of OH masers are seen along these same rims and thus indicate that shock interactions taking place between W28 and adjacent molecular clouds at these sites. The new *ROSAT* HRI mosaic image of W28 shows very starkly the centrally-concentrated X-ray morphology of the SNR and its strong anti-correlation with the shell-like radio morphology.

3) We have performed a spatially-resolved spectroscopic analysis of the *Chandra* observation of W28 where we have analyzed the spectra extracted from the bright central peak, several arcminute-scale regions near the central peak and annular regions centered on the bright peak. We have fit the spectrum of the peak with two VRNEI components: the fitted elemental abundances are subsolar, indicating that the emission from the peak is dominated by swept-up material rather than ejecta. Fits to the arcminute-scale regions with two VRNEI components produce generally consistent results with the fit to the spectra of the central peak region: in these fits, we find evidence for enhanced oxygen abundance relative to iron abundances. This result is expected for SNRs with massive stellar progenitors and – together with the evidence for an association with adjacent molecular clouds – further cements the interpretation that W28 arose from a massive stellar progenitor. Finally, we have fit spectra from concentric annular regions centered on the bright central peak to search for gradients in temperature and elemental abundances:

consistent with other MMSNRs, we find no evidence for a temperature gradient with increasing distance from the bright central peak. In contrast to prediction, we find no evidence for a gradient in elemental abundance either.

4) We have presented a comparison of the spatial morphologies of W28 at X-ray, optical and radio wavelengths. As the archetypical MMSNR, W28 features a shell-like radio morphology with a contrasting center-filled X-ray morphology with a thermal spectrum. The only spatial feature that is detected at all three wavelengths is the northeastern “ear”; this region appears to be a site of a particularly dramatic interaction between the W28 shock and an adjacent molecular cloud. In contrast to other MMSNRs, the optical morphology of W28 is not shell-like but instead center-filled; this may be due to the particularly complex interstellar medium conditions into which W28 is expanding.

5) We have analyzed the X-ray properties of two individual X-ray sources that stand out in the X-ray images: CXOU J175857.55–233400.3 (a hard X-ray source seen toward the southwest portion of W28 by prior *ASCA* observations of the SNR) and 3XMM J180058.5–232735 (a point-like X-ray source seen near the geometric center of the SNR). These sources have attracted interest as candidate X-ray-emitting neutron stars that may be associated with W28. Through an analysis of spectral properties (including fits to extracted X-ray spectra) and a search for counterparts at different wavelengths, we conclude that neither of these sources is a plausible candidate for a neutron star associated with W28. The former source is most likely to be a CV or a quiescent LMXB while the latter is most likely to be a coronally-active MS star.

We thank the anonymous referee for many useful comments that improved the quality of this manuscript. We thank G. Dubner for kindly sharing her radio image of W28 and Kazik Borkowski for helpful discussions about X-ray emission from SNRs. T.G.P. thanks Joseph DePasquale and the Chandra X-ray Center Help Desk Team in preparing the

exposure-corrected *Chandra* images of W28. T.G.P. also thanks Steven Snowden for his assistance in preparing the HRI mosaicked image of W28. This research has made use of data obtained from the High Energy Astrophysics Science Archive Research Center (HEASARC), provided by NASA's Goddard Space Flight Center. This research has also made use of NASA's Astrophysics Data System Bibliographic Services. PFW acknowledges support from the NSF under grant AST-0908566.

## REFERENCES

- Abdo, A. A. et al. 2010, *ApJ*, 718, 348
- Aharonian, F. et al. 2008, *A&A*, 481, 401
- Arikawa, Y., Tatematsu, K., Sekimoto, Y. & Takahashi, T. 1999, *PASJ*, 51, L7
- Arnaud, K. A. 1996, *Astronomical Data Analysis Software and Systems V*, eds. Jacoby G. and Barnes, J., p17, *ASP Conf. Series Volume 101*
- Borkowski, K. J., Lyerly, W. J. & Reynolds, S. P. 2001, *ApJ*, 548, 820
- Broersen, S. & Vink, J. 2015, *MNRAS*, 446, 3885
- Chen, Y., Su, Y., Slane, P. O. & Wang, Q. D. 2004, *ApJ*, 616, 885
- Chen, Y., Seward, F. D., Sun, M. & Li, J.-T. 2008, *ApJ*, 676, 1040
- Chevalier, R. A. 1999, *ApJ*, 511, 798
- Clark, D. H. & Caswell, J. L. 1976, *ApJ*, *MNRAS*, 174, 267
- Claussen, M. J., Frail, D. A. , Goss, W. M. & Gaume, R. A. 1997, *ApJ*, 489, 143
- Claussen, M. J., Goss, W. M., Frail, D. A. & Desai, K. 1999, *ApJ*, 522, 349
- Claussen, M. J., Goss, W. M., Desai, K. M. & Brogan, C. L. 2002, *ApJ*, 580, 909
- Clemens, D. P. 1985, *ApJ*, 295, 422
- Cox, D. P., Shelton, R. L., Maciejewski, W., Smith, R. K., Plewa, R., Pawl, A. & Rózyczka, M. 1999, *ApJ*, 524, 179
- Dubner, G. M., Velázquez, P. F., Goss, W. M. & Holdaway, M. A. 2000, *AJ*, 120, 1933

- Fesen, R. A., Winkler, F., Rathore, Y., Downes, R. A., Wallace, D. & Tweedy, R. W. 1997, *AJ*, 113, 767
- Frail, D. A., Kulkarni, S. R. & Vasisht, G. 1993, *Nature*, 365, 136
- Frail, D. A., Kassim, N. E. & Weiler, K. W. 1994, *AJ*, 107, 1120
- Frail, D. A., Goss, W. M. & Slysh, V. I. 1994b, *ApJ*, 424, L111
- Frail, D. A., Goss, W. M., Reynoso, E. M., Giacani, E. B., Green, A. J. & Otrupcek, R. 1996, *AJ*, 111, 1651
- Frail, D. A. & Mitchell, G. F. 1998, *ApJ*, 508, 690
- Freeman, P. E., Kashyap, V., Rosner, R. & Lamb, D. Q. 2002, *ApJS*, 138, 185
- Fruscione, A. et al. 2006, *Proc. SPIE*, 6720
- Goudis, C. 1976, *A&AS*, 45, 133
- Green, D.A., 2014, ‘*A Catalogue of Galactic Supernova Remnants (2014 May version)*’, Mullard Radio Astronomy Observatory, Cavendish Laboratory, Cambridge, United Kingdom (available on the World-Wide-Web at “<http://www.mrao.cam.ac.uk/surveys/snrs/>”).
- Hamuy, M., Walker, A. R., Suntzeff, N. B., Gigoux, P., Heathcote, S. R. & Phillips, M. M. 1992, *PASP*, 104, 533
- Hare, J., Rangelov, B., Sonbas, E., Kargaltsev, O. & Volkov, I. 2016, *ApJ*, 816, 52
- Harrus, I. M., Hughes, J. P., Singh, K. P., Koyama, K. & Asaoka, I. 1997, *ApJ*, 488, 781
- Hewitt, J. W., Yusef-Zadeh, F. & Wardle, M. 2008, *ApJ*, 683, 189
- Hoffman, I. M., Goss, W. M., Brogan, C. L. & Claussen, M. J. 2005, *ApJ*, 620, 257

- Jones, T. W. et al. 1998, *PASP*, 110, 125
- Kaspi, V. M., Lyne, A. G., Manchester, R. N., Johnston, S., D’Amico, N. & Shemar, S. L. 1993, *ApJ*, 409, L57
- Kassim, N. E. 1992, *AJ*, 103, 943
- Kawasaki, M., Ozaki, M., Nagase, F., Inoue, H. & Petre, R. 2005, *ApJ*, 631, 935
- Koo, B.-C., Rho, J., Reach, W. T., Jung, J. & Mangum, J. G. 2001, *ApJ*, 552, 175
- Kundu, M. R. 1970, *ApJ*, 162, 17
- Kundu, M. R. & Velusamy, T. 1972, *A&A*, 20, 237
- Lada, C.-J. 1987, *Star Forming Regions*, 115, 1.
- Lazendic, J. S. & Slane, P. O. 2006, *ApJ*, 647, 350
- Li, H. & Chen, Y. 2010, *MNRAS*, 409, 35
- Long, K., Blair, W. P., Matsui, Y. & White, R. L. 1991, *ApJ*, 373, 567
- Manchester, R. N., D’Amico, N. & Tuohy, I. R. 1985, *MNRAS*, 212, 975
- Marquez-Lugo, R. A. & Phillips, J. P. 2010, *MNRAS*, 407, 94
- Mavromataki, F., Papamastorakis, J., Paleologou, E. V. & Ventura, J. 2000, *A&A*, 353, 371
- Mavromataki, F., Xilouri, E. & Boumis, P. 2004, *A&A*, 426, 567
- Mavromataki, F., Xilouris, E. M. & Boumis, P. 2007, *A&A*, 461, 991
- McKee, C. F. 1982, in *Supernovae: A Survey of Current Research*, ed. M. J. Rees & R. J. Stoneham (NATO ASI Ser. C, 90; Dordrecht: Reidel), 433

- Miceli, M. 2011, *MmSAI*, 82, 709
- Milne, D. K. & Wilson, T. L. 1971, *A&A*, 10, 220
- Milne, D. K. 1979, *ApJ*, 32, 83
- Nakamura, R., Bamba, A., Ishida, M., Yamazaki, R., Tatematsu, K., Kohri, K., Pühlhofer, G., Wagner, S. J. & Sawada, Makato 2014, *PASJ*, 66, 62
- Neufeld, D. A. et al. 2007, *ApJ*, 664, 890
- Nomoto, K., Hashimoto, M., Tsujimoto, T., Thielemann, F.-K., Kishimoto, N., Kubo, Y. & Nakasato, N. 1997, *Nucl. Phys.*, 616, 79
- Orlando, S., Bocchino, F., Miceli, M., Reale, F. & Peres, G. 2009, *Memorie della Societa Astronomica Italiana Supplementi*, 13, 97
- Pannuti, T. G., Rho, J., Borkowski, K. J. & Cameron, P. B. 2010, *AJ*, 140, 1787
- Pannuti, T. G., Kargaltsev, O., Napier, J. P. & Brehm, D. 2014a, *ApJ*, 782, 102
- Pannuti, T. G., Rho, J., Heinke, C. O. & Moffitt, W. P. 2014b, *AJ*, 147, 55
- Pavlov, G. G., Kargaltsev, O., Wong, J. A. & Garmire, G. P. 2009, *ApJ*, 691, 458
- Petre, R., Kuntz, K. D. & Shelton, R. L. 2002, *ApJ*, 579, 404
- Petruk, O. 2001, *A&A*, 371, 267
- Reach, W. T. & Rho, J. 1996, *A&A*, 315, 277
- Reach, W. T. & Rho, J. 1998, *ApJ*, 507, L93
- Reach, W. T. & Rho, J. 2000, *ApJ*, 544, 843

- Rho, J. Petre, R., Pisarski, R. & Jones, L.R. 1996, “Röntgenstrahlung from the Universe”  
Conference Proceedings, eds. Zimmermann, H. U., Trümper, J. & Yorke, H., MPE  
Report 263, p.273-274
- Rho, J. & Petre, R. 1997, ApJ, 484, 828
- Rho, J. & Petre, R. 1998, ApJ, 503, L167
- Rho, J., Decourchelle, A. & Petre, R. 1998, BAAS, 193, 74.01
- Rho, J. & Borkowski, K. J. 2002, ApJ, 575, 201
- Rosen, S. R., Webb, N. A., Watson, M. G., et al. 2016, A&A, 590, A1
- Safi-Harb, S., Ogelman, H. & Finley, J. P. 1995, ApJ, 439, 722
- Sawada, M. & Koyama, K. 2012, PASJ, 64, 81
- Shaver, P. A. & Goss, W. M. 1970, Australian Journal. Phys. Astrophys. Suppl., 14, 77
- Shelton, R. L., Cox, D. P., Maciejewski, W., Smith, R. K., Plewa, T., Pawl, A. & Rózyczka,  
M. 1999, ApJ, 524, 192
- Shelton, R. L., Kuntz, K. D. & Petre, R., 2004 ApJ, 611, 906
- Smith, R. K., Brickhouse, N. S., Liedahl, D. A. & Raymond, J. C. 2001, ApJ, 556, L91
- Snowden, S. L. 1998, ApJS, 117, 233
- Sonbas, E., Rangelov, B., Kargaltsev, O., et al. 2016, ApJ, 821, 54
- Swartz, D. A., Pavlov, G. G., Clarke, T., et al. 2015, ApJ, 808, 84
- Vink, J. 2012, A&A Rev., 20, 49
- White, R. L. & Long, K. S. 1991, ApJ, 373, 543

Wilms, J., Allen, A. & McCray, R. 2000, 542, 914

Woosley, S. E. & Weaver, T. A. 1995, ApJS, 101, 181

Wooten, H. A. 1981, ApJ, 245, 105

Yusef-Zadeh, F., Wardle, M., Rho, J. & Sakano, M. 2003, ApJ, 585, 319

Zacharias, N., Urban, S. E., Zacharias, M. I., Hall, D. M., Wycoff, G. L., Rafferty, T. J.,  
Germain, M. E., Holdenried, E. R., et al. 2000, AJ, 120, 2131

Zacharias, N., Finch, C. T., Girard, T. M. et al. 2013, AJ, 145, 44

Zhang, G.-Y., Chen, Y., Su, Y., Zhou, X., Pannuti, T. G. & Zhou, P. 2015, ApJ, 799, 103

Zhou, P., Safi-Harb, S., Chen, Y. et al. 2014, ApJ, 791, 87

Zombeck, M. V., David, L. P., Harnden, F. R. & Kearns, K. 1995, Proc. SPIE, 2518, 304

Table 1. Summary of Optical Imaging Observations of W28

Designation	Filter		Exposure
	$\lambda_0$ (Å)	$\Delta\lambda^a$ (Å)	(s)
H $\alpha$	6568	28	$4 \times 600$
[S II] $\lambda\lambda 6716, 6731$	6728	50	$4 \times 600$
Red Continuum	6852	95	$4 \times 300$

<sup>a</sup>Full width at half maximum.

Table 2. Summary of *ROSAT* HRI and *Chandra* ACIS Observations of W28

Observatory and Instrument	Sequence Number	ObsID <sup>a</sup>	Nominal R.A. (J2000.0) (h m s)	Nominal Decl. (J2000.0) (° ' ")	Date	Effective Exposure Time <sup>b</sup> (seconds)	Sampled Portion of W28
<i>ROSAT</i> HRI	RH500382N00	–	18 00 48.0	–23 20 24.0	20 March 1995	23765	Center
<i>ROSAT</i> HRI	RH500382A01	–	18 00 48.0	–23 20 24.0	27 March 1996	11319	Center
<i>ROSAT</i> HRI	RH500484N00	–	18 01 19.2	–23 04 48.0	11 September 1998	27120	Northeast
<i>ROSAT</i> HRI	RH500485N00	–	17 59 14.4	–23 19 12.0	5 October 1997	15134	Northwest
<i>ROSAT</i> HRI	RH500486N00	–	18 01 43.2	–23 35 24.0	15 March 1998	3992	Southeast
<i>ROSAT</i> HRI	RH500486A01	–	18 01 43.2	–23 35 24.0	11 September 1998	14856	Southeast
<i>ROSAT</i> HRI	RH500487N00	–	18 00 19.2	–23 36 00.0	14 March 1998	14211	South
<i>ROSAT</i> HRI	RH500487A01	–	18 00 19.2	–23 36 00.0	8 September 1998	15300	South
<i>ROSAT</i> HRI	RH500488N00	–	17 59 00.0	–23 36 00.0	8 September 1998	6576	Southwest
<i>Chandra</i> ACIS	500278	2828	18 00 24.6	–23 25 55.7	12 October 2002	88994	Center and Southwest

<sup>a</sup>For the *Chandra* ACIS observation only.

<sup>b</sup>In the cases of the *ROSAT* HRI observations, the given exposure times are deadtime-corrected. Broken exposures (RH500382N00 and RH500382A01, RH500486N00 and RH500486A01, RH500487N00 and RH500487A01) have been combined into single datasets for the purposes of boosting the signal-to-noise and preparing a mosaicked *ROSAT* HRI image of W28. See Section 2.2.

Table 3. Summary of Fits to Extracted *Chandra* Spectrum of Central Region<sup>a</sup>

Parameter	TBABS× (VAPEC+VAPEC)	TBABS× (VNEI+VNEI)	TBABS× VRNEI	TBABS× (VRNEI+VRNEI)
$N_H$ ( $10^{22}$ cm <sup>-2</sup> )	0.43±0.02	0.41 <sup>+0.03</sup> <sub>-0.02</sub>	0.50±0.02	1.14 <sup>+0.09</sup> <sub>-0.12</sub>
$kT_{e1}$ (keV)	0.65±0.01	0.68±0.01	0.61 <sup>+0.02</sup> <sub>-0.01</sub>	0.10±0.01
$kT_{Z1}$ (keV)	...	...	10.31 <sup>+13.94</sup> <sub>-4.02</sub>	0.16 <sup>+0.02</sup> <sub>-0.01</sub>
$\tau_1$ ( $10^{11}$ cm <sup>-3</sup> s)	...	4.51 <sup>+0.42</sup> <sub>-0.51</sub>	6.24 <sup>+0.42</sup> <sub>-0.51</sub>	<1.24
Normalization <sub>1</sub> <sup>b</sup> (cm <sup>-5</sup> )	$3.38 \times 10^{-3}$	$2.69 \times 10^{-3}$	$7.41 \times 10^{-3}$	0.60
$kT_{e2}$ (keV)	1.70 <sup>+0.17</sup> <sub>-0.14</sub>	1.81 <sup>+0.39</sup> <sub>-0.18</sub>	...	0.42 <sup>+0.05</sup> <sub>-0.04</sub>
$kT_{Z2}$ (keV)	...	...	...	3.08 <sup>+2.86</sup> <sub>-0.97</sub>
$\tau_2$ ( $10^{11}$ cm <sup>-3</sup> s)	...	5.75 <sup>+7.12</sup> <sub>-3.06</sub>	...	5.55 <sup>+0.49</sup> <sub>-0.63</sub>
Normalization <sub>2</sub> <sup>b</sup> (cm <sup>-5</sup> )	$7.79 \times 10^{-4}$	$8.31 \times 10^{-4}$	...	$1.65 \times 10^{-2}$
Abundances <sup>c</sup>				
O	1 (frozen)	1.32 <sup>+0.25</sup> <sub>-0.26</sub>	0.55 <sup>+0.15</sup> <sub>-0.14</sub>	0.62 <sup>+0.26</sup> <sub>-0.19</sub>
Ne	1.44 <sup>+0.11</sup> <sub>-0.14</sub>	1 (frozen)	0.54±0.10	0.59 <sup>+0.14</sup> <sub>-0.13</sub>
Mg	1 (frozen)	1 (frozen)	0.72 <sup>+0.05</sup> <sub>-0.07</sub>	1 (frozen)
Fe	0.45±0.02	0.51 <sup>+0.04</sup> <sub>-0.03</sub>	0.33 <sup>+0.04</sup> <sub>-0.03</sub>	0.40 <sup>+0.07</sup> <sub>-0.05</sub>
$\chi^2/\text{DOF}$	326.18/180	316.07/178	310.10/178	205.00/175
$\Delta\chi^2$	1.81	1.78	1.74	1.17

<sup>a</sup>For the energy range 0.5-4.0 keV. All quoted errors are at the 90% confidence level.

<sup>b</sup>Defined in units of  $(10^{-14}/4\pi d^2) \int n_e n_p dV$ , where  $d$  is the distance to the source (in cm),  $n_e$  and  $n_p$  are the number densities of electrons and hydrogen nuclei, respectively (in units of cm<sup>-3</sup>) and finally  $\int dV$  is the integral over the entire volume of the X-ray-emitting plasma (in units of cm<sup>-3</sup>).

<sup>c</sup>Relative to solar.

Table 4. Summary of Fits to Extracted Spectra of Five ACIS-S3 Regions and ACIS-S4 Region with TBABS×VNEI Model<sup>a</sup>

Parameter	Region 1	Region 2	Region 3	Region 4	Region 5	ACIS-S4 Region
$kT_e$ (keV)	$0.64^{+0.01}_{-0.02}$	$0.75^{+0.03}_{-0.04}$	$0.69^{+0.01}_{-0.02}$	$0.67^{+0.03}_{-0.02}$	$0.69 \pm 0.01$	$0.66 \pm 0.01$
O <sup>b</sup>	$3.55^{+0.95}_{-0.79}$	$4.59^{+1.22}_{-1.63}$	$4.67^{+1.42}_{-1.28}$	$6.79^{+1.12}_{-1.03}$	$8.69^{+0.68}_{-0.67}$	$4.28^{+0.77}_{-0.82}$
Fe <sup>b</sup>	$0.59 \pm 0.06$	$0.78^{+0.17}_{-0.07}$	$0.71^{+0.10}_{-0.14}$	1.00 (frozen)	1.00 (frozen)	$0.57^{+0.05}_{-0.06}$
$\tau$ ( $10^{11} \text{ cm}^{-3} \text{ s}^{-1}$ )	>10	$4.24^{+1.22}_{-1.09}$	$4.68^{+1.11}_{-0.75}$	$4.43^{+1.24}_{-0.96}$	$3.82^{+0.43}_{-0.49}$	$4.31^{+0.70}_{-0.27}$
Normalization <sup>c</sup> ( $\text{cm}^{-5}$ )	$8.09 \times 10^{-4}$	$3.14 \times 10^{-4}$	$5.91 \times 10^{-4}$	$3.11 \times 10^{-4}$	$1.14 \times 10^{-3}$	$2.89 \times 10^{-3}$

<sup>a</sup>All spectra were extracted over the energy range 0.5-4.0 keV except for the ACIS-S4 region, which was extracted over the energy range 0.6-2.0 keV. All quoted errors are at the 90% confidence level. The column densities for each spectrum were tied together with a fitted value of  $N_{\text{H}} = 0.65 \pm 0.02 \times 10^{22} \text{ cm}^{-2}$ . For this fit,  $\chi^2/\text{DOF} = \Delta\chi^2 = 1077.45/622 = 1.73$ .

<sup>b</sup>Relative to solar.

<sup>c</sup>Defined in units of  $(10^{-14}/4\pi d^2) \int n_e n_p dV$ , where  $d$  is the distance to the source (in cm),  $n_e$  and  $n_p$  are the number densities of electrons and hydrogen nuclei, respectively (in units of  $\text{cm}^{-3}$ ) and finally  $\int dV$  is the integral over the entire volume of the X-ray-emitting plasma (in units of  $\text{cm}^{-3}$ ).

Table 5. Summary of Fits to Extracted Spectra of Five ACIS-S3 Regions and ACIS-S4 Region with TBABS×VRNEI Model<sup>a</sup>

Parameter	Region 1	Region 2	Region 3	Region 4	Region 5	ACIS-S4 Region
$kT_e^b$ (keV)	0.65±0.01	0.67±0.04	0.63±0.02	0.68±0.03	0.63±0.02	0.62±0.01
$kT_Z^c$ (keV)	>5	7.14 (>2.54)	6.46 (>2.17)	>5	5.11 <sup>+8.78</sup> <sub>-2.71</sub>	>5
O <sup>d</sup>	2.47 <sup>+0.73</sup> <sub>-0.57</sub>	1.00 (frozen)	1.00 (frozen)	3.28 <sup>+1.69</sup> <sub>-1.05</sub>	2.05 <sup>+0.45</sup> <sub>-0.37</sub>	1.48 <sup>+0.27</sup> <sub>-0.30</sub>
Fe <sup>d</sup>	0.46 <sup>+0.05</sup> <sub>-0.04</sub>	0.45 <sup>+0.10</sup> <sub>-0.08</sub>	0.39 <sup>+0.07</sup> <sub>-0.04</sub>	0.65 <sup>+0.13</sup> <sub>-0.09</sub>	0.49 <sup>+0.08</sup> <sub>-0.04</sub>	0.36 <sup>+0.02</sup> <sub>-0.04</sub>
$\tau$ ( $10^{11} \text{ cm}^{-3} \text{ s}^{-1}$ )	>10 <sup>12</sup>	6.95 <sup>+2.22</sup> <sub>-3.87</sub>	7.86 <sup>+2.10</sup> <sub>-1.63</sub>	>10 <sup>12</sup>	6.94 <sup>+1.19</sup> <sub>-1.08</sub>	>10 <sup>12</sup>
Normalization <sup>e</sup> ( $\text{cm}^{-5}$ )	$8.25 \times 10^{-3}$	$5.36 \times 10^{-4}$	$9.99 \times 10^{-4}$	$4.03 \times 10^{-4}$	$2.24 \times 10^{-3}$	$4.01 \times 10^{-3}$

<sup>a</sup>The extracted spectra for the annular regions located on the ACIS-S3 chip were fitted over the energy range 0.5-4.0 keV while the extracted spectrum for the region on the ACIS-S4 chip were fitted over the energy range 0.6-2.0 keV. All quoted errors are at the 90% confidence level. The column densities for each spectrum were tied together with a fitted value of  $N_H = 0.57 \pm 0.01 \times 10^{22} \text{ cm}^{-2}$ . For this fit,  $\chi^2/\text{DOF} = \Delta\chi^2 = 1024.64/616 = 1.66$ .

<sup>b</sup>The electron temperature.

<sup>c</sup>The ion temperature.

<sup>d</sup>Relative to solar.

<sup>e</sup>Defined in units of  $(10^{-14}/4\pi d^2) \int n_e n_p dV$ , where  $d$  is the distance to the source (in cm),  $n_e$  and  $n_p$  are the number densities of electrons and hydrogen nuclei, respectively (in units of  $\text{cm}^{-3}$ ) and finally  $\int dV$  is the integral over the entire volume of the X-ray-emitting plasma (in units of  $\text{cm}^{-3}$ ).

Table 6. Summary of Fits to Extracted Spectra of Five ACIS-S3 Regions and ACIS-S4 Region with TBABS×(VRNEI+VRNEI) Model

Parameter	Region 1	Region 2	Region 3	Region 4	Region 5	ACIS-S4 Region
$kT_{e1}^b$ (keV)	0.19±0.02	0.08 (>0.10)	0.19 <sup>+0.08</sup> <sub>-0.04</sub>	0.08 (<0.10)	0.21 <sup>+0.01</sup> <sub>-0.02</sub>	0.41 <sup>+0.07</sup> <sub>-0.08</sub>
$kT_{Z1}^c$ (keV)	1.83(>1.12)	0.19 <sup>+0.19</sup> <sub>-0.02</sub>	>5	>5	>2.90	0.74±0.06
$\tau_1$ ( $10^{11}$ cm <sup>-3</sup> s)	7.49(±0.94)	<10	>10	10.29 <sup>+1.75</sup> <sub>-1.70</sub>	6.76 <sup>+0.60</sup> <sub>-0.67</sub>	<0.01
Normalization <sub>1</sub> <sup>d</sup> (cm <sup>-5</sup> )	6.27×10 <sup>-3</sup>	6.46×10 <sup>-3</sup>	3.68×10 <sup>-4</sup>	1.22×10 <sup>-2</sup>	7.69×10 <sup>-3</sup>	1×10 <sup>-3</sup>
$kT_{e2}^b$ (keV)	0.60 <sup>+0.08</sup> <sub>-0.10</sub>	0.56 <sup>+0.06</sup> <sub>-0.08</sub>	0.64 <sup>+0.01</sup> <sub>-0.02</sub>	0.35 <sup>+0.05</sup> <sub>-0.04</sub>	0.67 <sup>+0.05</sup> <sub>-0.04</sub>	0.34 <sup>+0.02</sup> <sub>-0.01</sub>
$kT_{Z2}^c$ (keV)	3.76 <sup>+7.81</sup> <sub>-1.89</sub>	3.66 (>1.39)	>5	2.08 <sup>+36.87</sup> <sub>-0.55</sub>	3.49 <sup>+3.50</sup> <sub>-1.46</sub>	>5
$\tau_2$ ( $10^{11}$ cm <sup>-3</sup> s)	5.19 <sup>+2.27</sup> <sub>-1.30</sub>	5.74 <sup>+1.79</sup> <sub>-2.26</sub>	>10	2.77 <sup>+1.99</sup> <sub>-0.75</sub>	5.81 <sup>+1.42</sup> <sub>-1.08</sub>	>10
Normalization <sub>2</sub> <sup>d</sup> (cm <sup>-5</sup> )	7.90×10 <sup>-4</sup>	8.03×10 <sup>-4</sup>	7.44×10 <sup>-4</sup>	1.16×10 <sup>-3</sup>	1.29×10 <sup>-3</sup>	6.21×10 <sup>-3</sup>
Abundances <sup>e</sup>						
O	0.48 <sup>+0.31</sup> <sub>-0.18</sub>	1.00 (frozen)	3.60 <sup>+0.89</sup> <sub>-0.80</sub>	1.00 (frozen)	1.00 (frozen)	1.38 <sup>+0.35</sup> <sub>-0.27</sub>
Ne	0.49 <sup>+0.29</sup> <sub>-0.24</sub>	1.00 (frozen)	2.08 <sup>+0.40</sup> <sub>-0.37</sub>	0.67 <sup>+0.31</sup> <sub>-0.22</sub>	1.00 (frozen)	0.64 <sup>+0.16</sup> <sub>-0.17</sub>
Fe	1.00 (frozen)	0.40 <sup>+0.16</sup> <sub>-0.10</sub>	1.00 (frozen)	1.00 (frozen)	1.23 <sup>+0.31</sup> <sub>-0.20</sub>	0.47±0.06

<sup>a</sup>The extracted spectra for the regions located on the ACIS-S3 chip were fitted over the energy range 0.5-4.0 keV while the extracted spectrum for the region on the ACIS-S4 chip were fitted over the energy range 0.6-2.0 keV. All quoted errors are at the 90% confidence level. The column densities for each spectrum were tied together with a fitted value of  $N_H = 0.88 \pm 0.03 \times 10^{22}$  cm<sup>-2</sup>. For this fit,  $\chi^2/\text{DOF} = \Delta\chi^2 = 734.87/692 = 1.24$ .

<sup>b</sup>The electron temperature.

<sup>c</sup>The ion temperature.

<sup>d</sup>Defined in units of  $(10^{-14}/4\pi d^2) \int n_e n_p dV$ , where  $d$  is the distance to the source (in cm),  $n_e$  and  $n_p$  are the number densities of electrons and hydrogen nuclei, respectively (in units of cm<sup>-3</sup>) and finally  $\int dV$  is the integral over the entire volume of the X-ray-emitting plasma (in units of cm<sup>-3</sup>).

<sup>e</sup>Relative to solar.

Table 7. Summary of TBABS×VRNEI Fits to Extracted Spectra for Annular Regions of ACIS-S3 Chip and ACIS-S4 Chip Region<sup>a</sup>

Parameter	1	2	3	4	5	6	7	8	S4 Chip Region
$kT_e$ <sup>b</sup>	0.62±0.01	0.65 <sup>+0.02</sup> <sub>-0.01</sub>	0.64±0.01	0.62±0.01	0.64±0.01	0.65±0.02	0.64±0.01	0.66 <sup>+0.02</sup> <sub>-0.01</sub>	0.62±0.01
$kT_z$ <sup>c</sup>	3.53 <sup>+2.68</sup> <sub>-1.59</sub>	3.25 <sup>+7.92</sup> <sub>-0.72</sub>	>4.47	4.55 <sup>+2.53</sup> <sub>-2.43</sub>	5.54 <sup>+2.57</sup> <sub>-1.90</sub>	4.47 <sup>+2.21</sup> <sub>-1.30</sub>	5.09 <sup>+2.28</sup> <sub>-0.80</sub>	6.65 <sup>+4.24</sup> <sub>-2.34</sub>	>5.00
O <sup>d</sup>	1.00 <sup>e</sup>	1.81 <sup>+0.32</sup> <sub>-0.37</sub>	1.29 <sup>+0.11</sup> <sub>-0.26</sub>	1.00 (frozen)	1.20 <sup>+0.09</sup> <sub>-0.20</sub>	1.52 <sup>+0.18</sup> <sub>-0.19</sub>	1.40 <sup>+0.12</sup> <sub>-0.10</sub>	1.57 <sup>+0.32</sup> <sub>-0.24</sub>	1.45 <sup>+0.22</sup> <sub>-0.23</sub>
Fe <sup>d</sup>	0.37±0.03	0.40±0.04	0.43 <sup>+0.05</sup> <sub>-0.02</sub>	0.35±0.02	0.36 <sup>+0.03</sup> <sub>-0.02</sub>	0.37 <sup>+0.02</sup> <sub>-0.03</sub>	0.34 <sup>+0.01</sup> <sub>-0.02</sub>	0.36 <sup>+0.03</sup> <sub>-0.04</sub>	0.35 <sup>+0.01</sup> <sub>-0.03</sub>
$\tau$ (10 <sup>11</sup> cm <sup>-3</sup> s)	6.21 <sup>+0.68</sup> <sub>-1.07</sub>	6.40 <sup>+1.64</sup> <sub>-0.78</sub>	7.45 <sup>+1.40</sup> <sub>-0.97</sub>	6.14 <sup>+0.53</sup> <sub>-0.44</sub>	7.15 <sup>+0.73</sup> <sub>-0.70</sub>	6.95 <sup>+0.47</sup> <sub>-0.54</sub>	6.98 <sup>+0.61</sup> <sub>-0.30</sub>	7.44 <sup>+0.87</sup> <sub>-0.66</sub>	>20
Normalization <sup>e</sup> (10 <sup>-3</sup> cm <sup>-5</sup> )	1.65	2.13	2.86	3.90	4.14	4.45	5.18	5.42	4.03

<sup>a</sup>The extracted spectra for the annular regions located on the ACIS-S3 chip were fitted over the energy range 0.5-4.0 keV while the extracted spectrum for the region on the ACIS-S4 chip were fitted over the energy range 0.6-2.0 keV. All quoted errors are at the 90% confidence level. The column densities for each spectrum were tied together with a fitted value of  $N_H = 0.57 \pm 0.01 \times 10^{22}$  cm<sup>-2</sup>. For this fit,  $\chi^2/\text{DOF} = \Delta\chi^2 = 2394.02/1379 = 1.74$ .

<sup>b</sup>The electron temperature.

<sup>c</sup>The ion temperature.

<sup>d</sup>Relative to solar.

<sup>e</sup>Defined in units of  $(10^{-14}/4\pi d^2) \int n_e n_p dV$ , where  $d$  is the distance to the source (in cm),  $n_e$  and  $n_p$  are the number densities of electrons and hydrogen nuclei, respectively (in units of cm<sup>-3</sup>) and finally  $\int dV$  is the integral over the entire volume of the X-ray-emitting plasma (in units of cm<sup>-3</sup>).

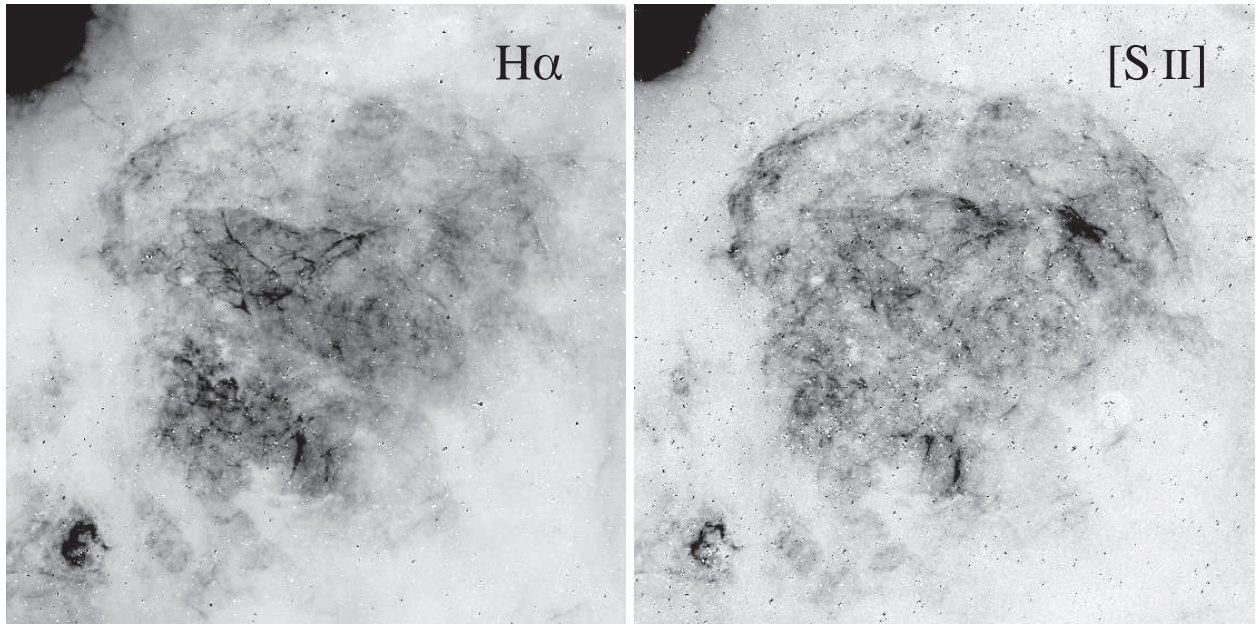


Fig. 1.— Images of W28 in  $H\alpha$  (left) and  $[S II] \lambda\lambda 6716,6731$  emission lines, taken from the Burrell Schmidt telescope at KPNO. A continuum image has been scaled and subtracted from each. The field is  $45'$  square, oriented north up and east left. The bright source seen toward the upper left is a portion of M20 (the Trifid Nebula).

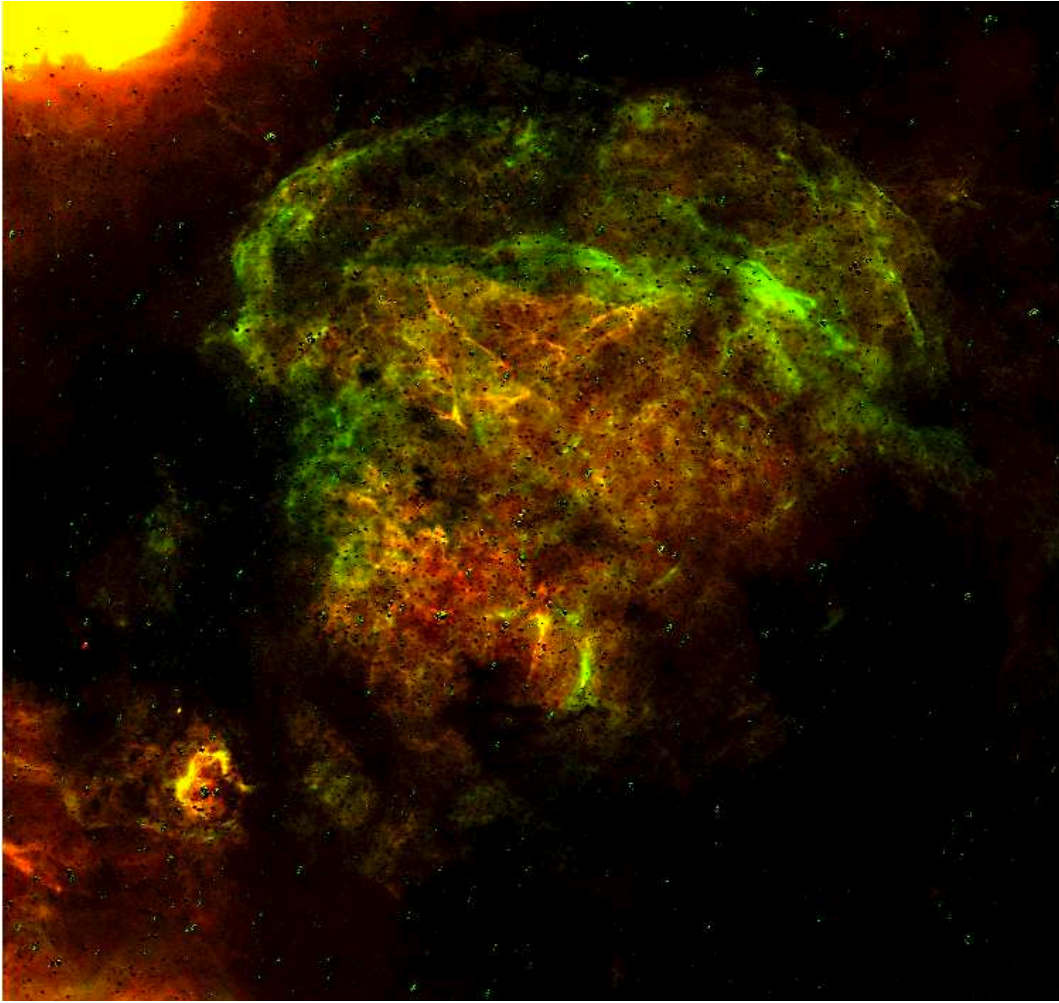


Fig. 2.— Two-color optical image of W28:  $H\alpha$  emission is shown in red, and [S II] in green. The continuum-subtracted images are the same as in Fig. 1, but the field is somewhat larger,  $50'$  square.

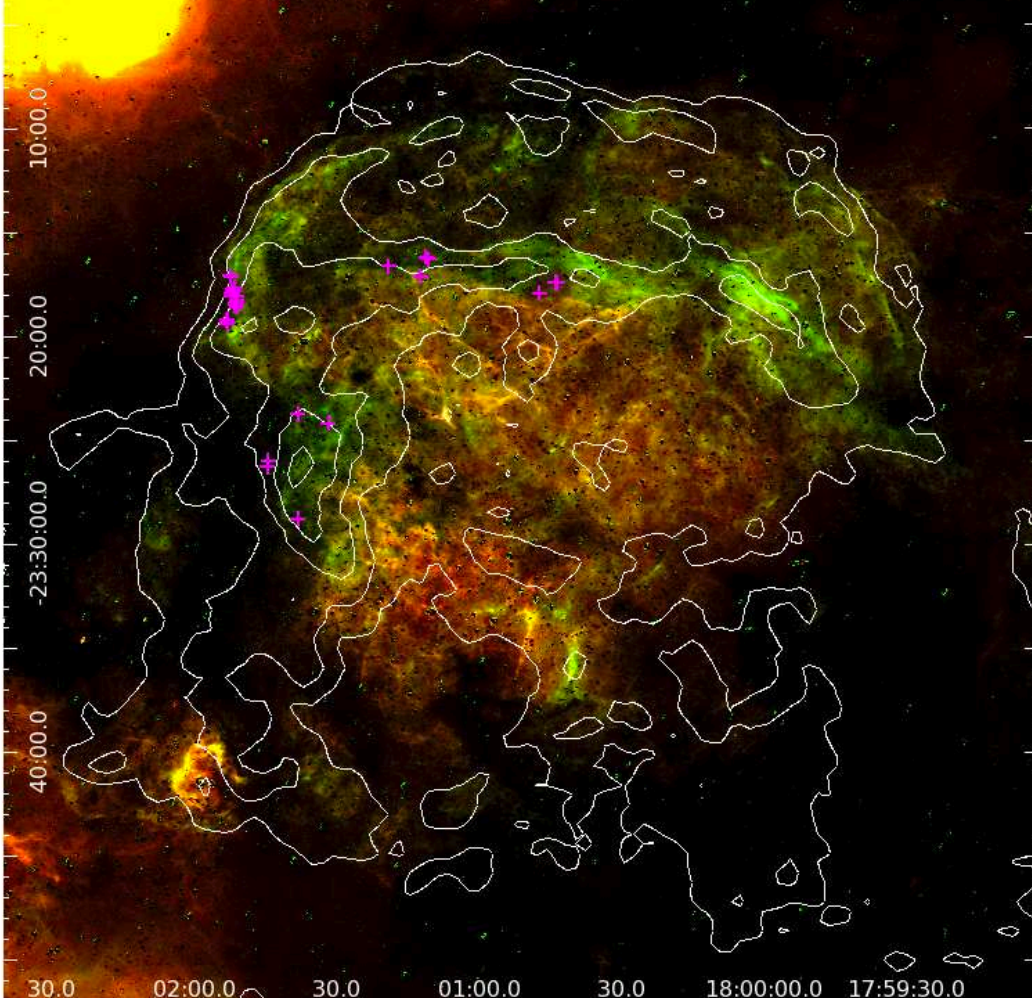


Fig. 3.— The same color image shown in Fig. 2, with contours from the 1415 MHz radio image (Dubner et al. 2000) overlaid for comparison. The contour levels are 0.002, 0.012, 0.022, 0.032 and 0.042 Jy/beam. The locations of OH masers (Claussen et al. 1999) are shown as magenta crosses: these masers are associated with interactions between SNRs and molecular clouds. Note that the [S II] emission is concentrated along the eastern and northern radio rim of the SNR, and that the masers are preferentially correlated with the regions of [S II] emission.

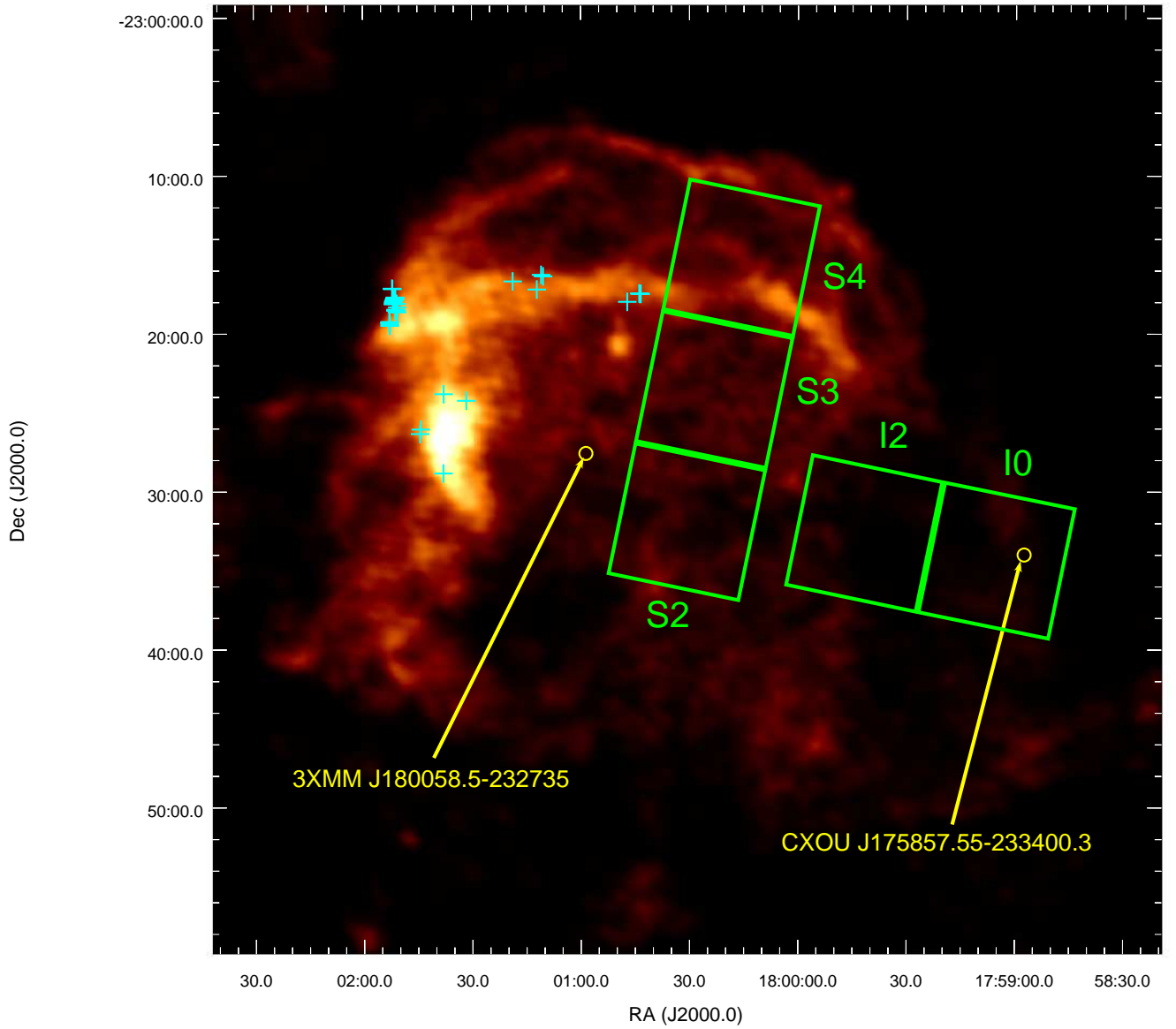


Fig. 4.— Radio map of W28 made with the VLA (Dubner et al. 2000). The green squares denote the footprints of the ACIS chips during the *Chandra* observation of this SNR. The cyan crosses indicate the locations of the 1720 MHz OH masers detected by Claussen et al. (1999) and the yellow circles indicate the locations of the discrete X-ray sources 3XMM J180058.5–232735 and CXOU J175857.55–233400.3 (see Section 4).

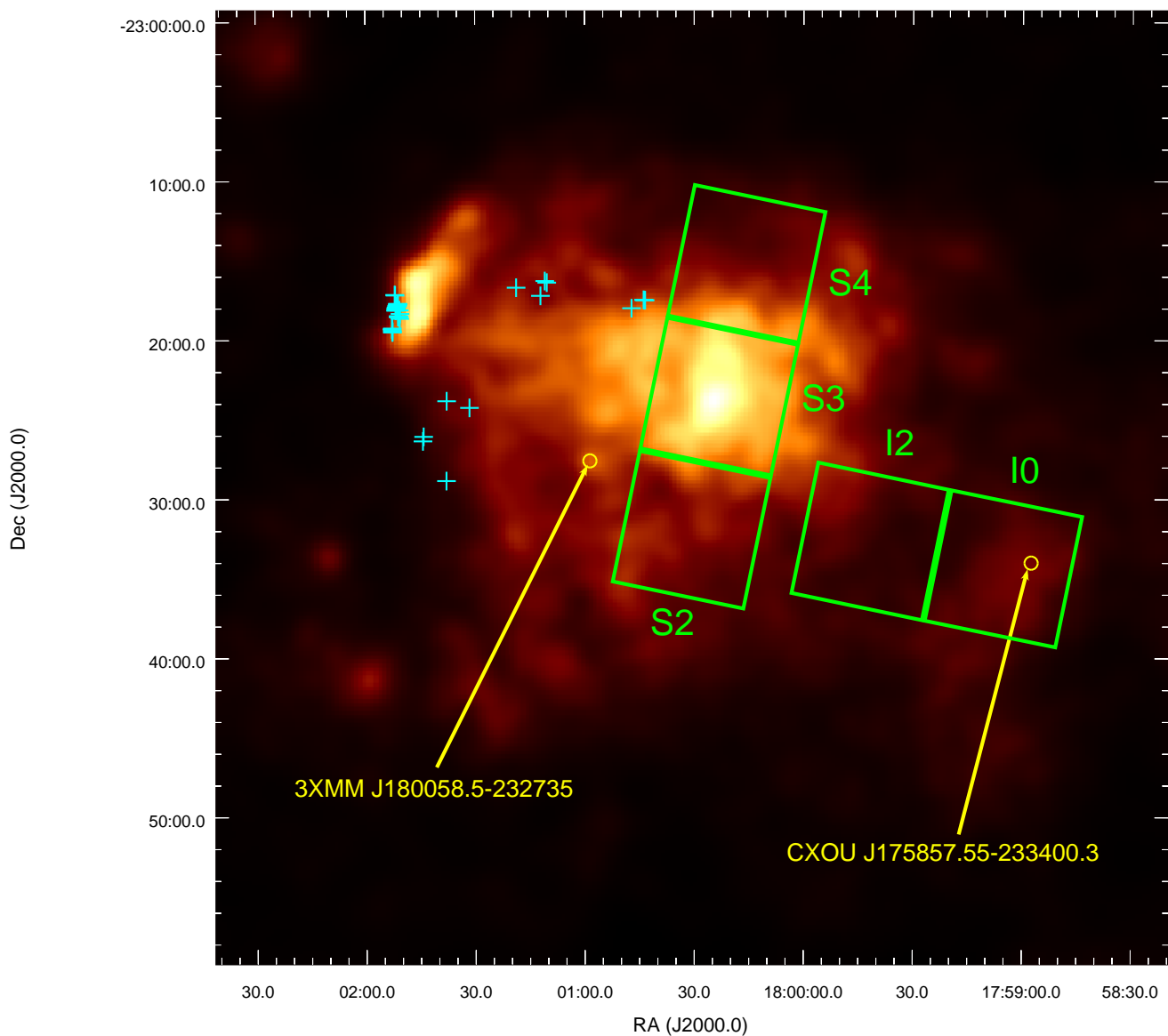


Fig. 5.— *ROSAT* PSPC image of W28 (Rho & Borkowski 2002). Similar to Figure 4, the locations of the footprints of the ACIS chips, the OH masers and the locations of discrete X-ray sources discussed in Section 4 are indicated. Notice the centrally-concentrated X-ray morphology of W28 in contrast to the shell-like radio morphology depicted in Figure 4: these contrasting morphologies characterize MMSNRs.

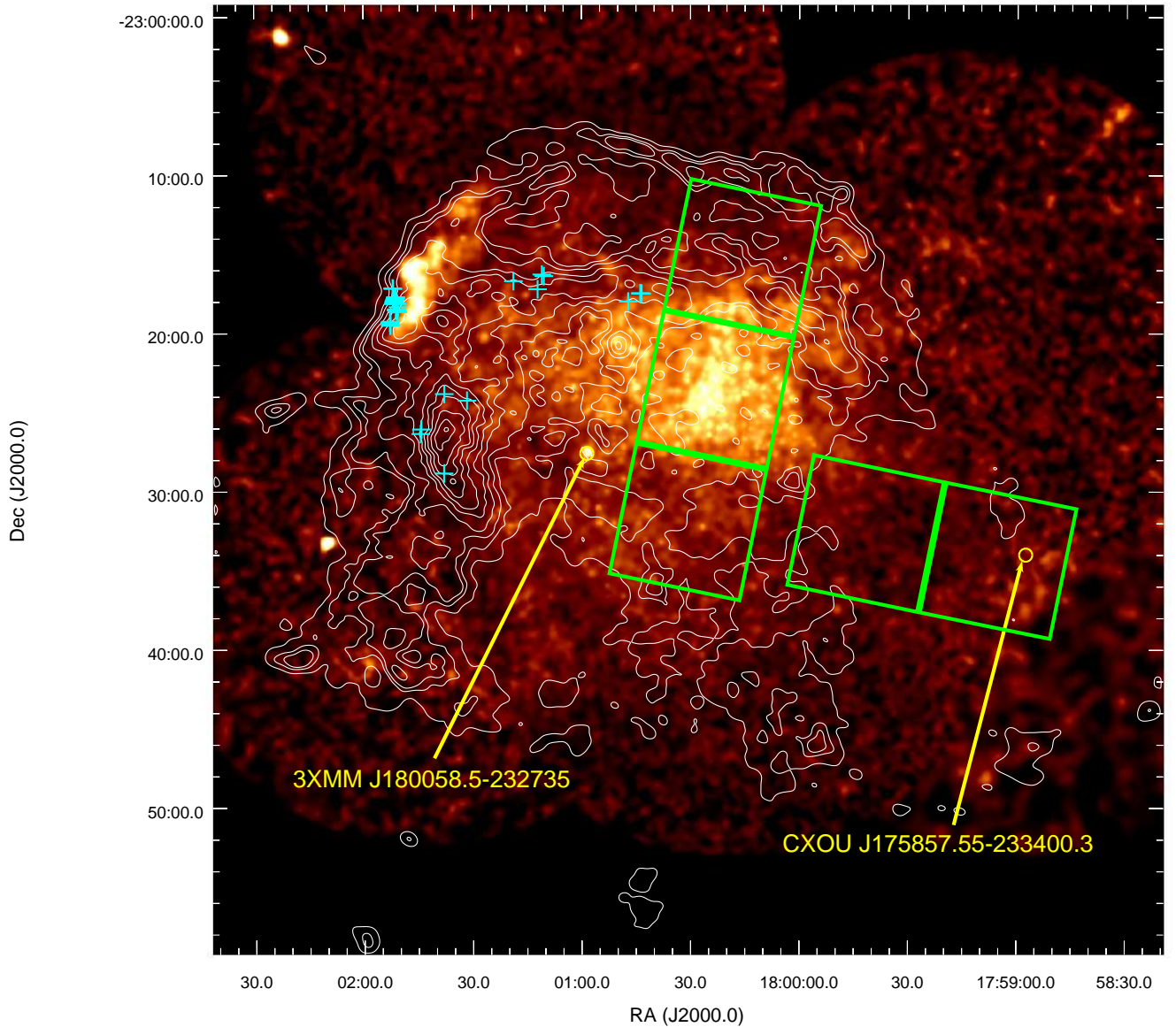


Fig. 6.— Adaptively-smoothed (with a smoothing kernel of 30 counts) *ROSAT* HRI mosaic of W28 as prepared from the set of HRI observations listed in Table 2. Radio emission from W28 is depicted using overlaid white contours: these contours have been placed at the levels of 0.0035, 0.0075, 0.01, 0.015, 0.02, 0.025, 0.03, 0.035, 0.041, 0.0475, 0.05375 and 0.06 Jansky/beam. Similar to Figure 4, the locations of the footprints of the ACIS chips, the OH masers and the locations of discrete X-ray sources discussed in Section 4 are indicated. The contrasting X-ray and radio morphologies of W28 are again apparent in this figure.

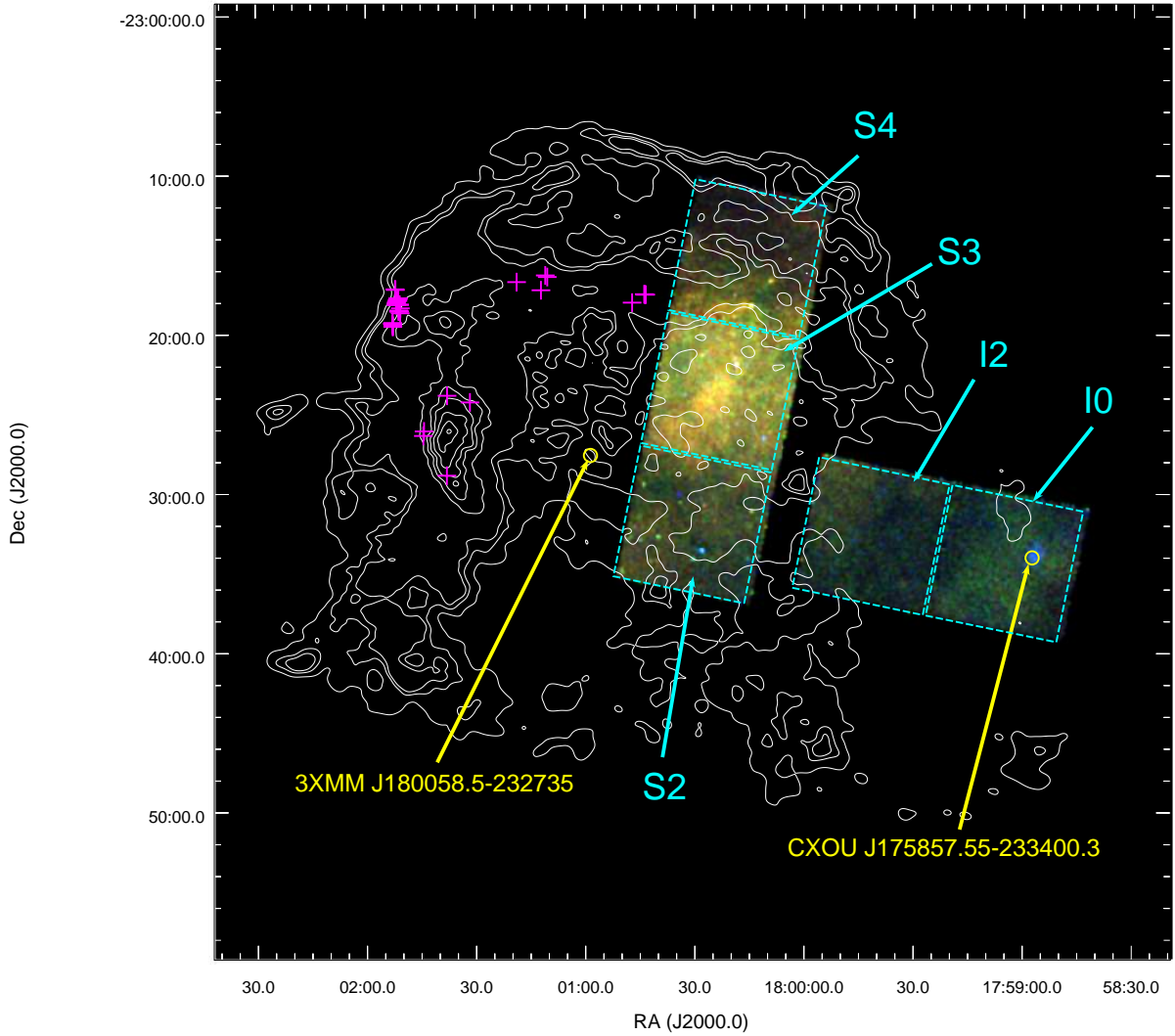


Fig. 7.— Adaptively smoothed *Chandra* ACIS image of W28. Soft (0.5 keV - 1.2 keV), medium (1.2 keV - 2.0 keV) and hard (2.0 keV - 7.0 keV) emission is shown in red, green and blue, respectively. The red contours correspond to radio emission detected by the VLA at a frequency of 1415 MHz: the contour levels are 0.0035, 0.0075, 0.01, 0.023, 0.03, 0.035, 0.041, 0.0475, 0.5375 and 0.06 Jansky/beam. The green crosses show the locations of the 1720 MHz OH masers detected by Claussen et al. (1999).

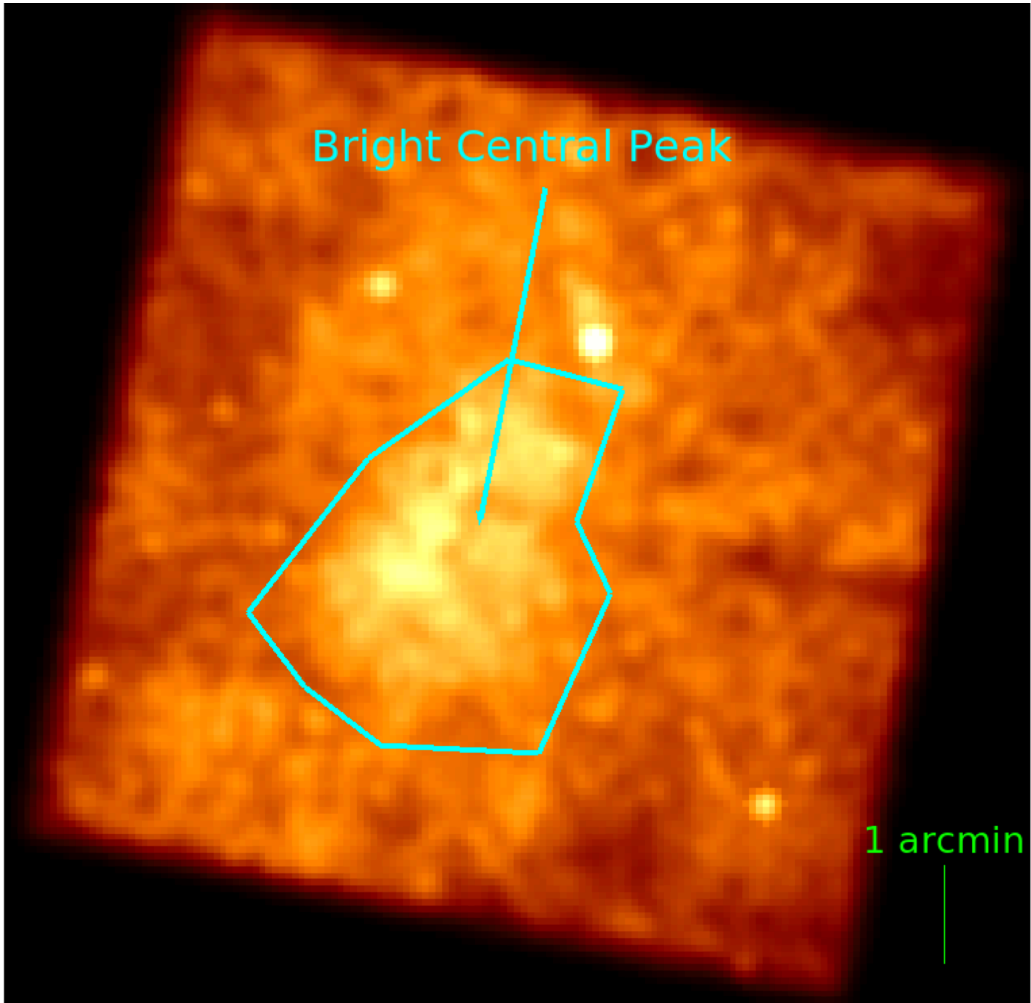


Fig. 8.— *Chandra* ACIS-S3 broadband (0.5 keV - 7.0 keV) exposure-corrected and smoothed image of the central portion of W28. The region of spectral extraction for the bright central peak is indicated.

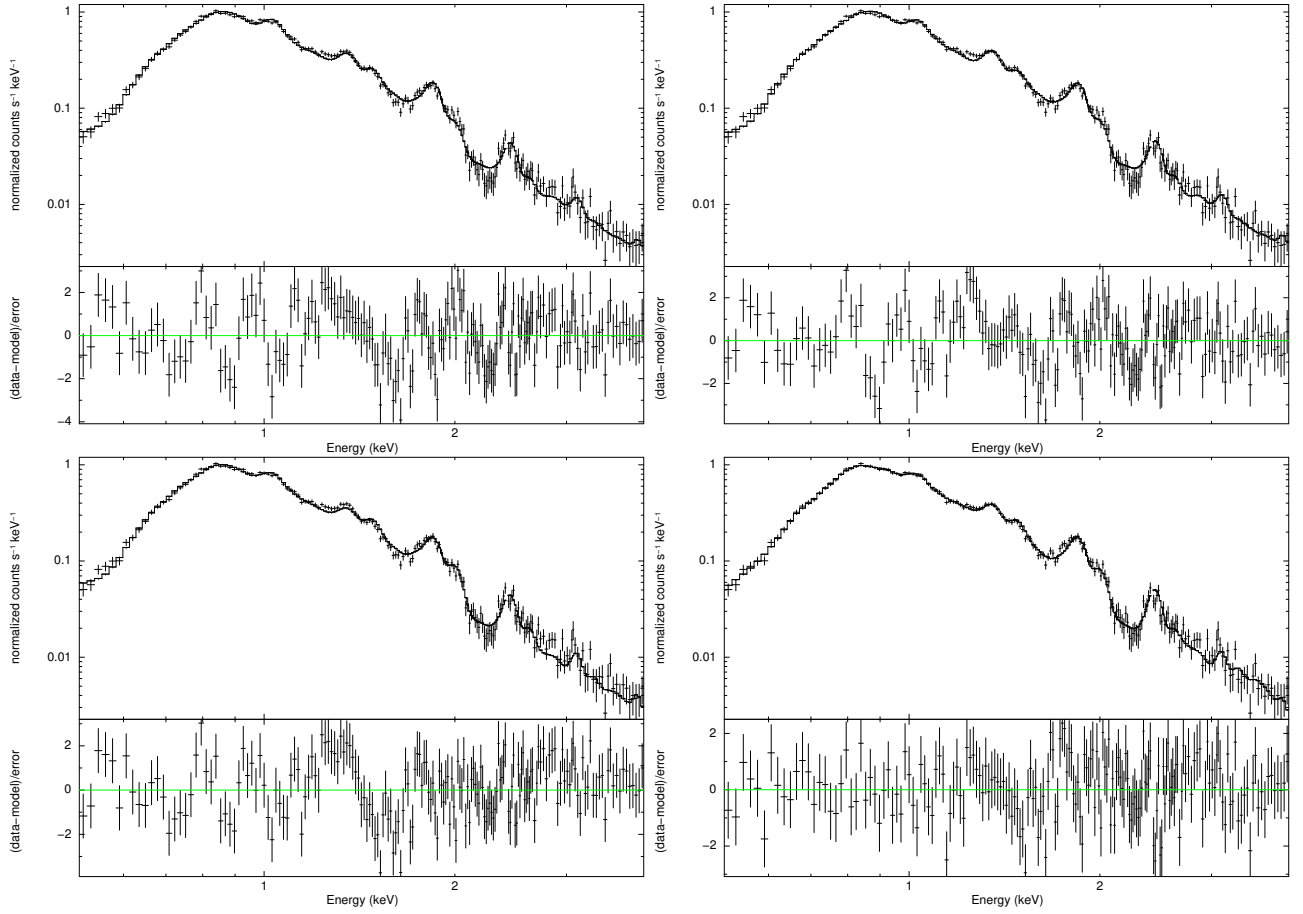


Fig. 9.— Four spectral fits to the extracted spectrum of the central bright emission region of W28. The parameters of these fits are listed in Table 3. Upper left:  $\text{TBABS} \times (\text{VAPEC} + \text{VAPEC})$  fit. Upper right:  $\text{TBABS} \times (\text{VNEI} + \text{VNEI})$  fit. Lower left:  $\text{TBABS} \times \text{VRNEI}$ . Lower right:  $\text{TBABS} \times (\text{VRNEI} + \text{VRNEI})$ .

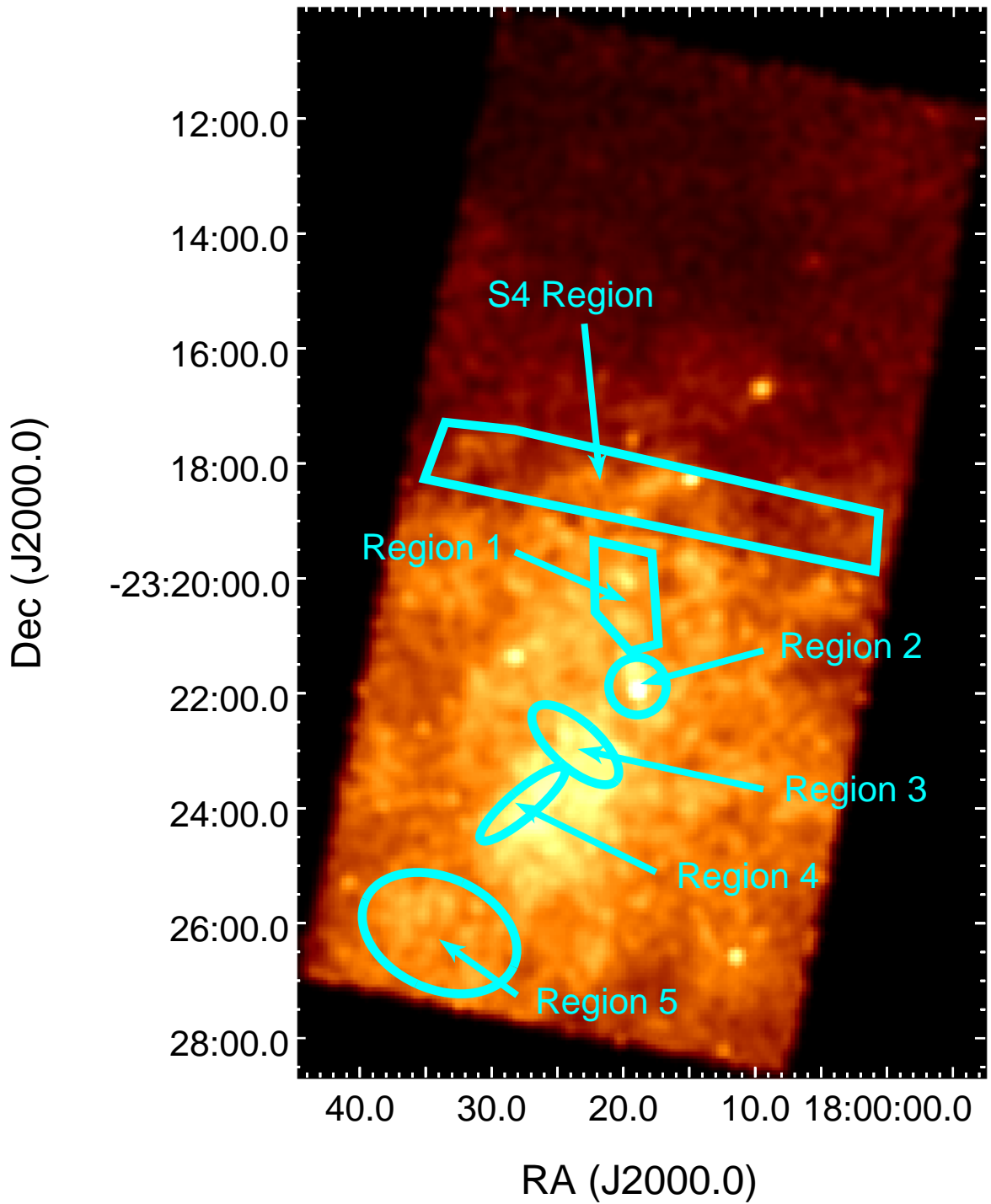


Fig. 10.— An exposure-corrected image of the ACIS-S3 and ACIS-S4 chips over the broad energy range (0.7 - 5.0 keV). The five regions of spectral extraction on the ACIS-S3 chip and the region of spectral extraction on the ACIS-S4 chip are indicated.

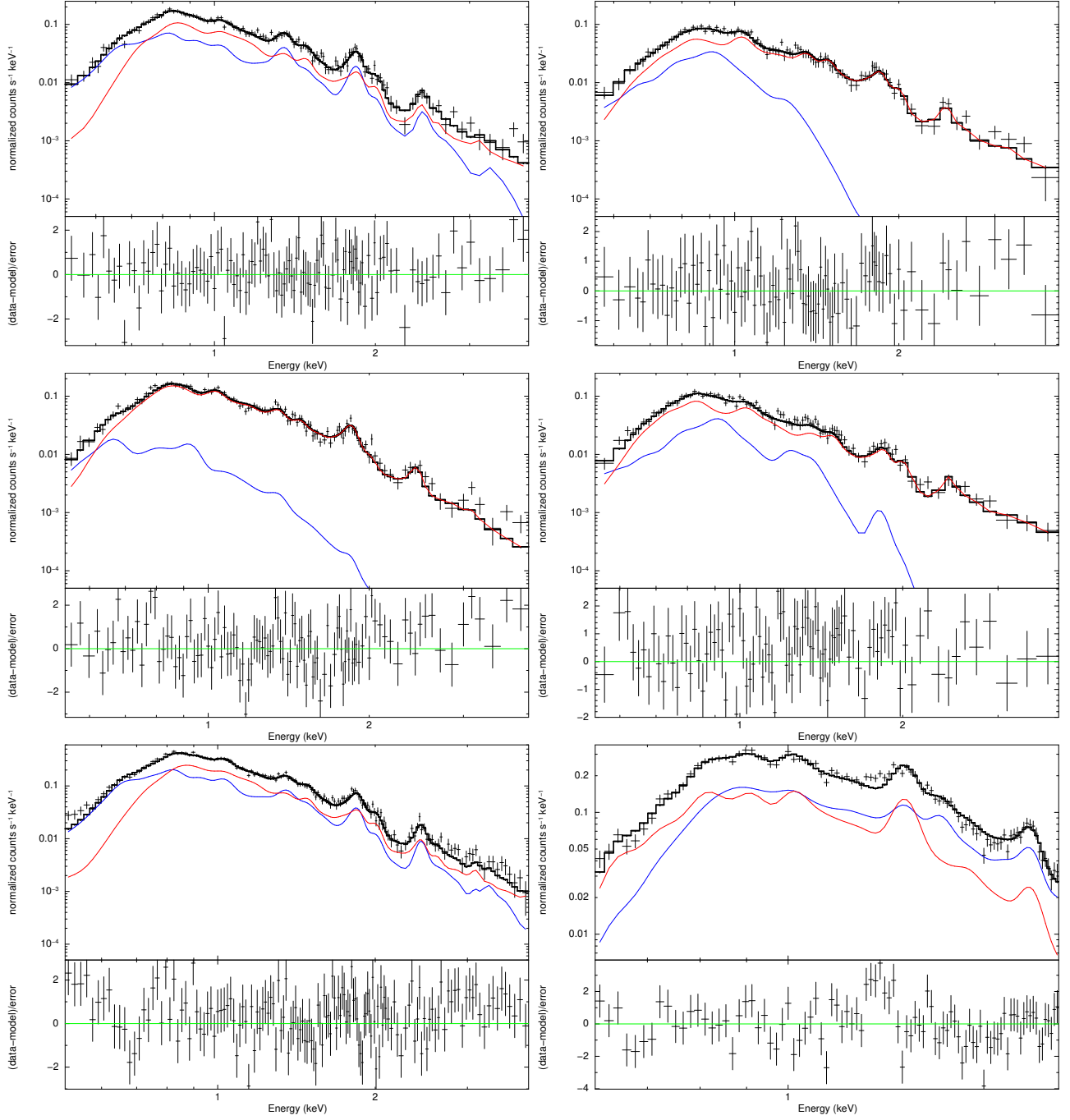


Fig. 11.— Fits to the extracted spectra of the five ACIS-S3 regions and the ACIS-S4 region using a  $\text{TBABS} \times (\text{VRNEI} + \text{VRNEI})$  model: the parameters of the fits to these models are given in Table 6. In these images, the emission from the  $kT_{e1}$  and  $kT_{z1}$  component is shown in blue while the emission from the  $kT_{e2}$  and  $kT_{z2}$  component is shown in red. Upper left: Region 1. Upper right: Region 2. Middle left: Region 3. Medium right: Region 4. Bottom left: Region 5. Bottom right: ACIS-S4 region.

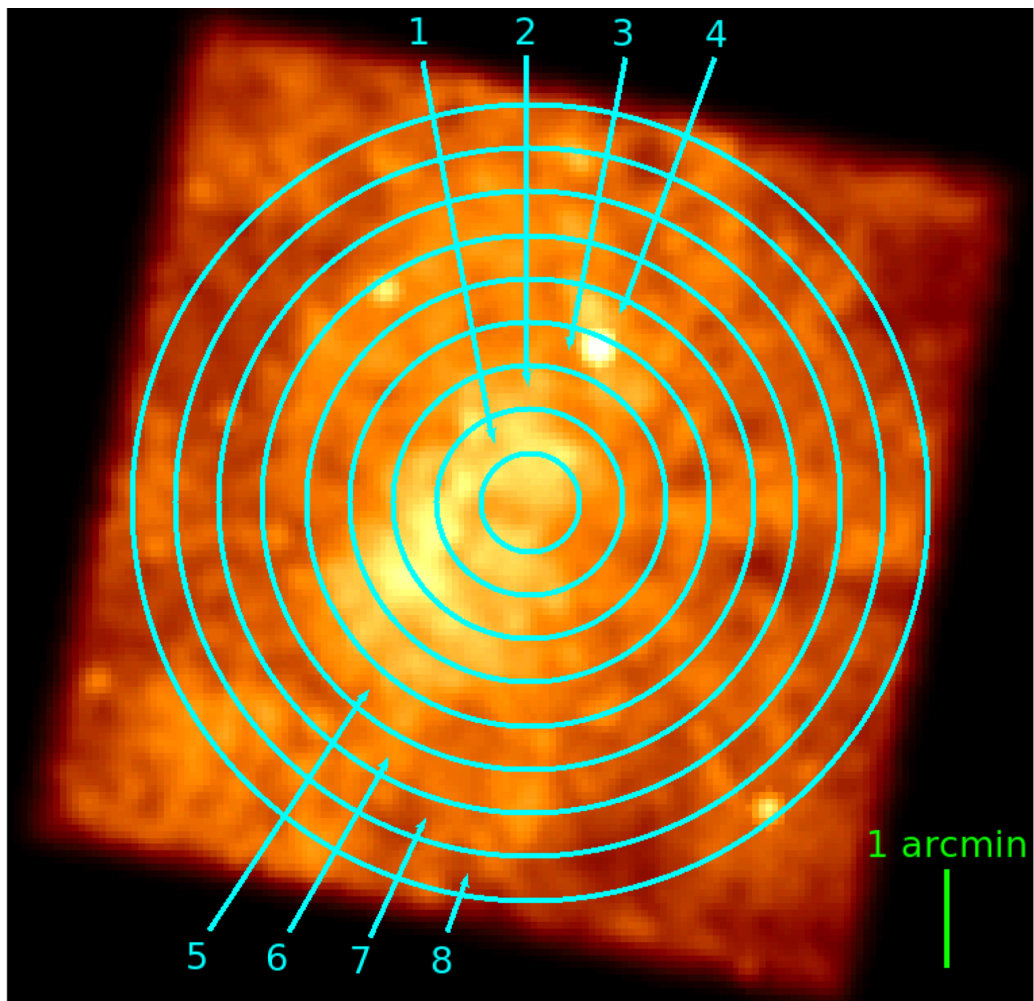


Fig. 12.— Same as Figure 8 but with the annular regions of spectral extraction indicated.

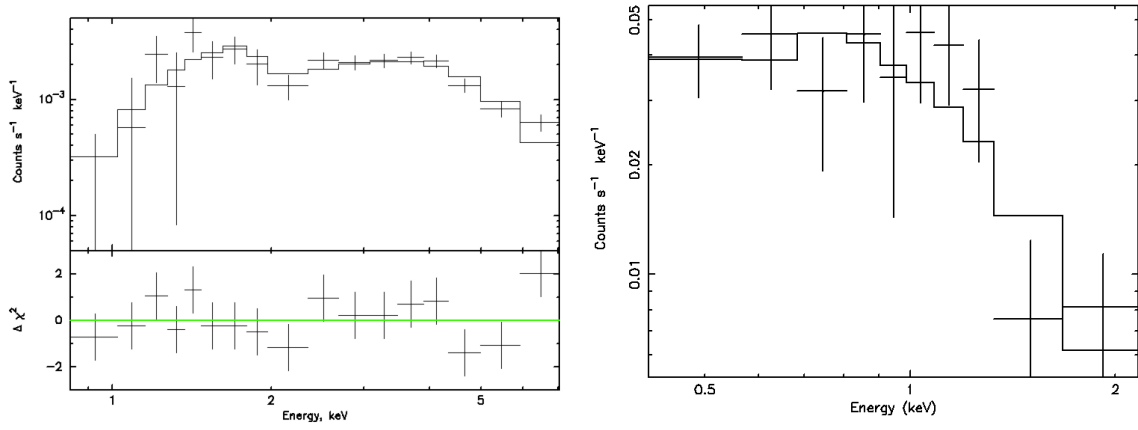


Fig. 13.— The ACIS spectrum of CXOU J175857.55–233400.3 (left) and the EPIC-PN spectrum of 3XMM J180058.5–232735 (right). Both spectra are fitted with an absorbed power law model (see Section 4).

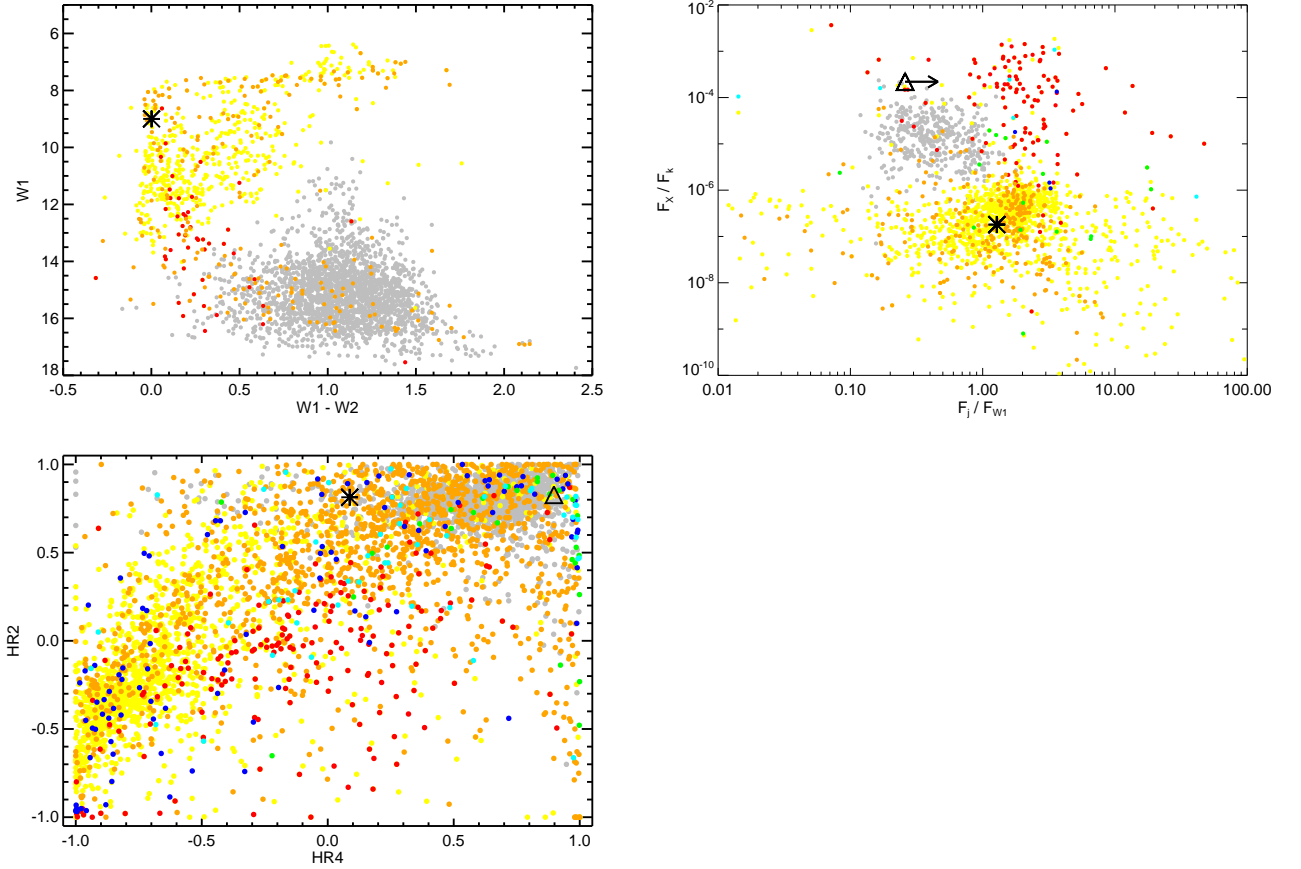


Fig. 14.— *WISE* color-color diagram (upper left),  $F_j/F_{W1}$  vs.  $F_X/F_k$  flux diagram (upper right) and HR4 vs. HR2 hardness ratio diagram (lower left) diagrams. The plotted black triangles and asterisks corresponds to the locations of of CXOU J175857.55–233400.3 and 2XMM J180058.6–232724 = 3XMM J180058.5–232735, respectively. The arrow indicates a lower limit. Other symbols are AGN (gray), Stars (yellow), YSOs (orange), CVs (red), pulsars (blue), HMXBs (green) and LMXBs (cyan) based on the training dataset described in Sonbas et al. (2016).

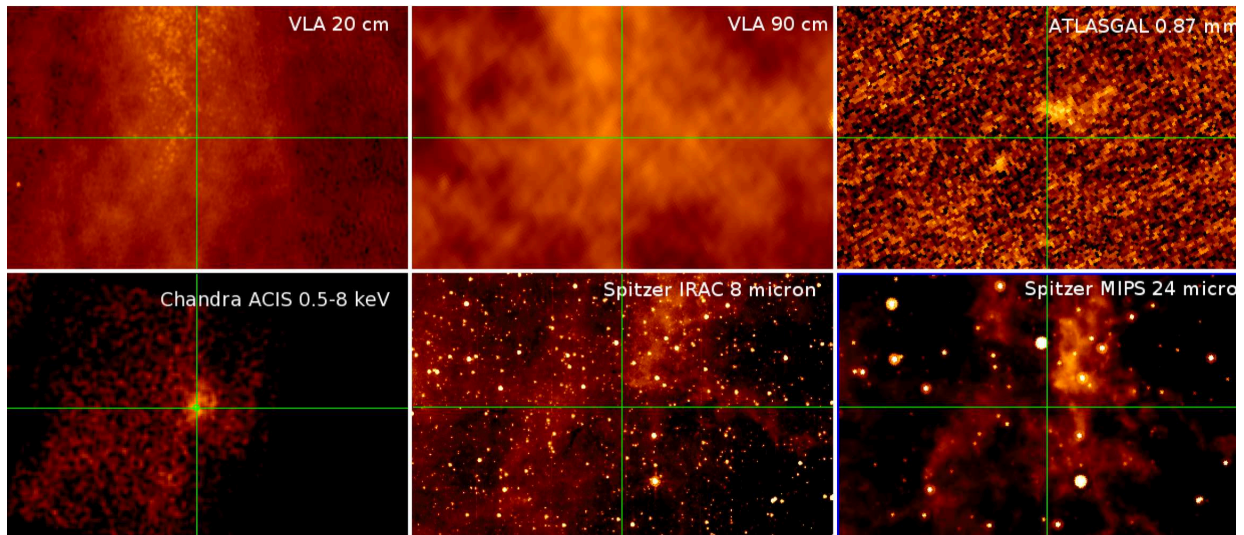


Fig. 15.— The vicinity of the CXOU J175857.55–233400.3 at different wavelengths. The source position is indicated by crosshairs in all panels.